A QUANTITATIVE THERMAL IMAGING TECHNIQUE TO EXTRACT A CROSS-STREAM SURFACE VELOCITY PROFILE FROM A FLOWING BODY OF WATER

A Thesis

Presented to the Faculty of the Graduate School

of Cornell University

In Partial Fulfillment of the Requirements for the Degree of

Master of Science

by

Chad Stuart Helmle

May 2005

ABSTRACT

The United States Geological Survey (USGS) is responsible for monitoring river flow rates at over 7,000 locations across the United States. This operation is expensive, inefficient, and often dangerous, as USGS personnel must deploy direct in-the-field measurement equipment to obtain the required flow data during storm events. An affordable, remote, non-contact sensor that is capable of determining river flow rates under a variety of flow environments is, therefore, highly desired by the USGS and other agencies worldwide charged with the task of water flow monitoring and management.

A technique is presented in which a cross-stream surface velocity profile is extracted from a series of thermal infrared images of a flowing water surface. Analytical methods and algorithms are borrowed from Quantitative Imaging (QI) fields such as Particle Image Velocimetry (PIV) and Particle Tracking Velocimetry (PTV), and are adapted for use on the thermographic image set. Monte Carlo Simulations are used to compare several iterative improvements to the initial correlation-based displacement algorithm. Particular emphasis is placed upon extracting reliable results from images with a very low signal-to-noise ratio (SNR) typical of the image type recorded by an inexpensive thermal imaging system in the nearly uniform temperature environment of interest.

Laboratory experiments are used to verify the capacity of the altered displacement algorithm to extract cross-stream velocity profiles from thermal images recorded from above an open-channel flume. Several cases ranging from high to low SNR are studied. The displacement algorithm's analysis of the high SNR data sets provides a velocity profile that agrees with the profile measured by an Acoustic Doppler Velocimeter (ADV). Displacement results for the medium and low SNR

cases required further processing after the initial displacement algorithm analysis. A qualitative analysis of the post-processed data reveals that a deterministic signal can be extracted from such noisy image sets, and further refinements of the displacement algorithms to accomplish these tasks are possible.

BIOGRAPHICAL SKETCH

The author was born in Lawrence, Kansas in 1975. He began college in 1993 at the University of Notre Dame and received his Bachelor's degree in Engineering and Environmental Science in 1997. He was immediately commissioned as a 2nd Lieutenant in the United States Air Force where he spent the next five years serving as a Civil Engineering Officer. In 2002, he separated at the rank of Captain and enrolled in the graduate school at Cornell University as a Master's of Science candidate. Over the past two and a half years, he has focused his academic research on QI-based remote sensing in environmental fluid mechanics. He is currently employed as an associate research specialist at the University of California, Santa Barbara.

To my incredible wife, Jill, and my rambunctious son, Beck

ACKNOWLEDGMENTS

So many people contributed to my efforts in finishing this thesis that there is no way to include them all here. It is only with their support logistically, intellectually, and emotionally that I was able to complete this project.

First and foremost, I would like to thank my advisor, Professor Edwin A. Cowen for recognizing my potential as a Master's Degree candidate and providing me with the opportunity to accomplish my goal of earning that degree. I consider myself fortunate to have been the individual that saw this idea of his to its initial fruition and I look forward to working with him to further develop this technology. I would also like to acknowledge the other committee member, Professor Tammo Steenhuis, who was gracious and trusting enough to take me on as a minor advisee despite his incredibly busy schedule.

I must recognize Professor Phillip L-F. Liu for the extra time he dedicated to my understanding of the incredibly complex subject matter that he teaches in his classes, and Professor Wilfried Brutsaert and Professor Jean-Yves Parlange for their wisdom and their dazzling repertoires of stories and anecdotes. Special thanks also go to Dr. Monroe Weber-Shirk for his support with laboratory software.

I would like to convey my appreciation to Cameron Wilkens for his quite competent computer support and also Lee Virtue and Paul Charles for their shop expertise. Many of my fellow graduate students in the Environmental Fluid Mechanics and Hydrology program provided me with daily support on a variety of issues. They are Qian Liao, Peter J. Rusello, Jon Lapsley, In Mei Sou, Gustavo Zarruck, Khaled Abdullah Al-Banaa and Alexandra King, among others. In particular, I must thank Evan Variano for listening to my rants at the gym, hearing out my ideas on PIV and providing positive feedback on many subjects throughout my time at

Cornell. And to my friend, Russ Dudley, thank you so much for spending hour upon hour helping me collect late-night data sets both in the lab and at other local establishments.

Acknowledgement must also go to the sponsor of this project, the National Science Foundation's Small Grant for Exploratory Research (SGER) program (grant no. CTS-341911).

And finally, I must thank my parents and my loving siblings for their own unique style of support in which they continually reminded me of their love by asking questions such as, "Aren't you done with that thing yet?!" Nobody deserves thanks, however, more than my wonderful wife, Jill, who paid the greatest price for this Master's Thesis. I truly could not have finished this without her love, support and guidance.

TABLE OF CONTENTS

LIST OF FIGURES

LIST OF TABLES

CHAPTER 1

INTRODUCTION

1.1 Motivation

An astonishing amount of engineering effort and resources are spent on building and maintaining sustainable water supplies to the world's communities. As the human population exponentially increases, further stressing the existing water resources and infrastructure, so too does the demand for a clean and reliable water supply. Many communities are forced to meet this demand with expensive, large scale solutions, such as transporting water over extremely long distances, establishing water recycling programs, desalinization, and actively catching and storing storm water runoff. In the United Sates alone, the water supply crisis of the southwestern states is a primary example of what lengths local and state governments are willing to go to in order to maintain a sufficient supply of clean water. Cities such as Los Angeles, Phoenix, and Las Vegas have built aqueducts that span thousands of miles to transport water from remote reservoirs, while several other cities on the west coast such as Monterey and San Diego are attempting to develop desalinization plants to meet the expanding need. These examples illustrate the intense interest in maintaining a sustainable and clean water supply and highlight the fact that water is an increasingly valuable commodity in today's society.

Despite the water resources engineering efforts put forth to achieve water supply sustainability, there remains one particular field in which little significant progress has been made: the development of a reliable method to continuously measure volumetric river discharge rates. Discharge rate measurements are crucial for making sound engineering decisions in the design and operation of water resources

facilities, the study of fate and transport of contaminants in the environment, and the calculation of flood water levels among other applications. While sophisticated current meter technologies exist today, their use is typically cost prohibitive, if not dangerous, given the large scale of many water resources engineering problems. For this reason, engineers often rely upon data that has been empirically extrapolated and fit to a numerical model.

Engineers in the U.S. desiring river discharge rate data typically face the choice of using information that has been collected by the United States Geological Survey (USGS) over the course of many years, or collecting the data manually using some sort of current meter technology. Two types of current meters that are often used are the Acoustic Doppler Velocimeter (ADV) and the Acoustic Doppler Current Profiler (ADCP). The ADV records fluid velocities at a single "point" (typical measurement volume of 1 cm^3). While these measurements can be very accurate, the effort required to obtain a suitable cross-sectional profile are significant and usually not practical. The ADCP records fluid velocities along a one-dimensional profile. This instrument can also be quite accurate, but due to current technological and logistical issues, obtaining data near the boundaries of a river flow can be extremely difficult. Both of these measurement techniques require submersing the equipment in the water and taking measurements in multiple locations along the cross-section of the stream. In a high-flow environment (typically the most desired data), this can be an extremely dangerous and impractical task. Risks to human life and equipment are often too high to tolerate. Additionally, if historical data is required, this method will likely be of no use.

As an alternative to taking direct current velocity measurements, the USGS maintains over 7,000 gaging stations on rivers throughout the United States. These gaging stations measure the "stage" (or water level) at individual locations on the

river. In addition to the stage information, engineers deploy to each site on a regular basis and record direct current velocity measurements using a current meter. With these two pieces of information, over time a "rating curve" is developed in which stage is directly related to discharge for that river at that particular location. This data is typically readily available to the public. Unfortunately, due to sometimes dynamic bathymetric profiles and rather sparse or non-existent flow data available to allow the extrapolation of the rating curve to high-volume events, discharge rates calculated with these curves can be in error ranging from 10 – 70%.

Given the important role that water resource management and engineering will play in determining the future sustainability of global communities, it has become imperative to develop a method to continuously, reliably, and accurately measure volumetric river discharge rates. As other environmental measurement techniques advance, the limiting factor in calculating the total load of contaminants and sediment in river outfall is often the overall flow rate. To address this issue, the USGS has developed the research committee Hydro 21. This group's stated goal is to "identify and evaluate new technologies and methods that might have the potential to change the paradigm in the USGS stream gaging program," primarily focusing on "non-contact methods" that could be used in routine river discharge monitoring by direct measurement of river cross-sectional area, water surface elevation, and water velocity distribution across the river (http://or.water.usgs.gov/hydro21/index.shtml). Taking one step toward that goal, this thesis investigates a promising new technique in which the scalar temperature pattern (STP) on a flowing water surface is thermographically imaged and tracked and a surface velocity profile is obtained.

This new technique will take advantage of the thermally diverse surface of a flowing body of turbulent water as it equilibrates with its surroundings. The momentum flux that takes place at the boundaries of a fluvial flow (primarily at the

river bed and the air/water interface) induces turbulence and, therefore, mixing within the water column. While the turbulent mixing tends to homogenize the thermal structure of the water column, the inevitable temperature heat flux at the air/water interface tends to counter this phenomenon. As each parcel of water from the well mixed water column arrives at the surface the heat exchange takes place rapidly, ultimately resulting in a thermally diverse air/water interface.

The advantage of having this thermal diversity on the flowing water surface becomes evident by sequentially thermographically imaging the surface. Given the proper resolution, spectral sensitivity, and dynamic range, this thermal diversity is visible to an infrared camera. Viewing these images, one can witness new parcels of water arriving at the surface, reaching thermal equilibrium with the air, and being displaced by other new parcels. As this phenomenon occurs, the water surface continues to move downstream, carrying each of the surface parcels with it. Since the overall STP maintains its general shape for a substantial amount of time, this movement can be visually detected and tracked by viewing the sequential images.

The goal of this thesis is to establish a method in which the adaptation of quantitative imaging (QI) algorithms commonly used in particle image velocimetry (PIV) can be used to determine a surface velocity profile on a flowing water surface using infrared thermography. Infrared images of flowing water are captured in a laboratory setting and several displacement algorithms are tested with Monte Carlo Simulation and thermographic images, eventually adapting the algorithms to enable maximum efficiency in determining a comprehensive surface velocity profile.

1.2 Literature Review

Significant research has been accomplished in recent years studying and testing different methods of non-contact river discharge measurement. Many of these techniques directly apply a hybrid of well-studied QI techniques such as PIV and particle tracking velocimetry (PTV) in the case of free surface flows. These velocimetry techniques rely on surface imaging to determine the two-dimensional flow fields in open channel flows, each with its own unique drawbacks and advantages. Weitbrecht et al. (2002) used an "off the shelf" PIV package to measure the two-dimensional surface velocity field and identify the dominant large coherent structures on a shallow laboratory flow. This method required heavy seeding of the surface with several different types of buoyant tracers ranging from polystyrene particles to wooden spheres. While the tracers are generally considered to satisfactorily trace the actual pathlines of the fluid flow, surface tension in some conditions can create a problem in which the particles tend to stick together, deviating from the true pathlines and hence misrepresenting the actual velocity of fluid movement. Further, these particles integrate over their wetted depth of submergence and are affected by any air-side motions (i.e., wind). This problem may be mostly overcome in the laboratory by using surfactants and carefully selecting particle materials, however the practicality of the overall method in the natural environment is questionable for a multitude of reasons, including cost effectiveness, environmental pollution, and reliability.

As an alternative to adding tracer particles to a flow, Creutin et al. (2002) successfully used natural light reflection off of surface deformations to determine the two-dimensional flow field. The images recorded were analyzed for brightness variation and a traditional correlation PIV algorithm was used to determine the desired

velocity vector field. Fujita and Tsubaki (2002) presented a variation on this concept by using a novel synthetic spatio-temporal technique developed to take full advantage of the assumption that the dominant velocity component is in the streamwise direction. The result of this non-correlation-based technique is a one-dimensional flow field across the surface of the channel with a higher spatial resolution in the lateral direction. While both of these tracerless methods are desirable because they require no manual seeding of the fluid surface there are some obvious and significant drawbacks. Since they depend entirely on light reflections off of the surface, these methods are less accurate when less sunlight is reflected. They will therefore be useless during night hours, in shaded areas, and even on overcast days.

A seemingly more robust method of non-contact surface velocimetry is presented by Nicolas et al. (1997). Like the above natural light reflection technique, this method requires no tracer particles. They used coherent high resolution radar to image the surface and used a spatio-temporal technique to develop a velocity vector field. Lee et al. (2002) and Mason et al. (2002) separately present a radar Doppler-shift based surface velocimetry technique using "binning" to define the two-dimensional flow field. Both of these seem to provide a solution to the problem of the inability to take velocity measurements in poor or low light. Yet, they all still suffer from what almost every other surface velocity measurement technique does: lack of insight into subsurface velocities. Additionally, these methods are biased by the shear from wind waves at the surface and have no way of obtaining subsurface velocities. These are problems that potentially may be solved with the use of sequential quantitative thermal imaging techniques.

Although velocimetry using thermographic images has scarcely been studied, some research has been accomplished on the related topics of Scalar Image Velocimetry (SIV) (Dahm et al., 1992; Su and Dahm, 1996; Pearlstein and Carpenter,

1995; Carpenter and Pearlstein, 1996), Correlation Image Velocimetry (CIV) (Tokumaru and Dimotakis, 1995), and Optical Flow (OF) (Quenot, 1992). The image analyses range from Direct Numerical Simulation (DNS) images of an arbitrary passive scalar in 2 and 3 dimensional flows, to laboratory images of known dye-laden flow regimes (Couette Flow, axis-symmetric turbulent jet, etc…), to satellite imagery of weather patterns on the surface of Jupiter. The cumulative results of these studies suggest that, among other methods, a QI-based algorithm may be used to determine *image*-flow velocity from images of a passive scalar in a fluid flow.

Hetsroni et al. (2001) successfully used both traditional PIV and Optical Flow (OF) algorithms to establish a flow field in the lower boundary layer of a fully developed and artificially heated open channel flow by thermally imaging a piece of foil on the outside of the lower boundary. The thermal diversity of the flow directly above the bottom boundary instantly heated the foil, creating a thermal pattern that could clearly be seen to advect downstream. The assumption that the scalar temperature field seen on the foil in the infrared could be treated as a proxy tracer for the fluid velocity was justified. While the techniques developed in this paper are helpful, they have not been applied on thermographic images of a flowing water surface.

In addition to temperature being a proxy tracer for fluid motion, researchers studying mass transfer phenomena at the air/water interface also use it as a tracer for gas exchange processes. As a result, a number of research efforts have used infrared thermography on water body surfaces to study and measure mass transfer velocities. Haussecker, et al (2002) successfully accomplished this measurement (among others) by sequentially imaging the ocean surface using an infrared camera. The images were used to verify existing models and theoretical predictions of surface temperature distributions. Additionally, although fluid flow velocities were not investigated, the

images reveal thermal structure on the ocean surface that may enable the use of a QI-based algorithm to make an accurate velocity measurement.

A similar study by Garbe et al (2003) uses high-resolution infrared thermography of a laboratory wind driven water surface to further investigate gas transfer processes. By developing a total derivative method and taking advantage of the brightness change constraint equation (BCCE – similar to the SIV methods), they are able to calculate surface renewal rates, verify surface temperature distributions, and estimate gas transfer velocities. As a byproduct of their effort to determine the total derivative of these image sequences, a velocity field estimate is obtained. Although the details are not presented in his paper, Garbe did not use a QI-based velocimetry technique and a detailed analysis of velocity errors was not presented.

The need for a robust, non-contact volumetric river flow measurement system has been established. By combining advances in QI displacement algorithms and the recent accomplishments of gas transfer studies involving thermographic imaging of flowing water surfaces, this thesis takes the first step in developing a breakthrough technology that integrates these techniques into a useable and practical surface velocity profile extraction method. The potential advantages that a quantitative thermographic image velocimetry system would provide make this initial investigation into this new technique worth while. Although far beyond the scope of this thesis, possible benefits of using this system include the fact that the information gathered in each image may provide crucial information on energy budget analysis and gas transfer rates, the ability to make uninterrupted river surface velocity measurements, and the potential insight into subsurface velocities by using feature tracking technology to measure the velocity of large parcels of hot or cold water traveling slower or faster than the surrounding surface water and linking them to a certain depth in the river.

CHAPTER 2

EXPERIMENTAL FACILITIES AND METHODS

Quantitatively measuring the surface velocity profile of a uniform fluid flow using sequential infrared thermography has scarcely been attempted. The use of QI algorithms as tools to accurately accomplish this measurement introduces a unique set of challenges which can be overcome by employing the techniques and methods described in this chapter. Key elements include introducing several methods of enhancing the signal-to-noise ratio (SNR) of the STPs recorded by an inexpensive infrared camera in a highly uniform temperature environment.

2.1 Experimental Facility

The experiments were carried out in the wide flume constructed in the DeFrees Hydraulics Laboratory at Cornell University. It is a recirculating type wide open channel flume allowing generation of spanwise meandering flow motions. As shown in figure (Figure 1) the flume consists of inlet, test and outlet sections. The test section is constructed entirely of glass panes allowing excellent optical access (essential for PIV and Laser Induced Fluorescence (LIF) measurements). It is 15 m in length, 2 m in width and the maximum water depth is 0.64 m. The flow is driven by two axial pumps and carried into the inlet section through two 0.406 m diameter PVC pipes beneath the facility. The rates of the two pumps can be controlled digitally, allowing individual flow rates to vary either periodically or randomly while maintaining a constant total flow rate, resulting in enhanced spanwise meandering motion with various length scales in the test section. In the present study, however, the flow rates of both pumps

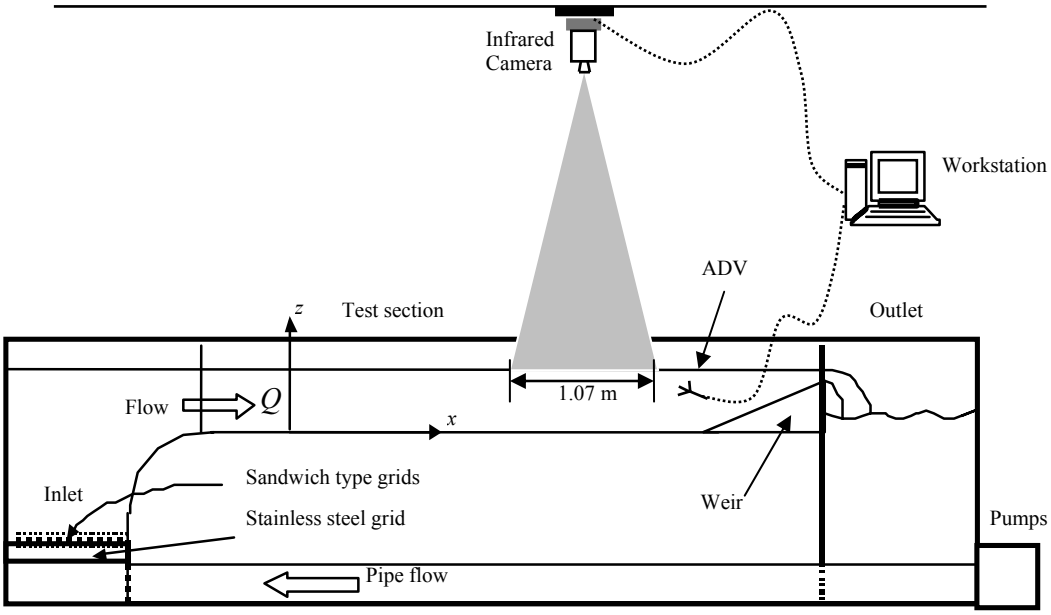

Figure 1: Experimental facility

are kept constant at 8 Hz and the depth was kept constant at 30 cm. The flow is conditioned in the inlet by a series of grids in a sandwich type construction. The grids are constructed of 5.1 cm deep stainless steel strap with 0.1 m × 0.1 m square openings. A 2.5 cm thick `horse hair' packing material layer is attached to the top of the steel grids. These materials are sandwiched between polypropylene molded thermoplastic mesh sheets. This series of grids is sufficient to break down large vortices generated by the two pumps and yields a quasi-homogeneous and isotropic turbulent flow. The turbulence is further conditioned by a nominally 4:1 contraction in the vertical before entering the test section. A 4 mm polycarbonate rod is mounted laterally along the junction between the inlet and test section to trip the boundary layer turbulence. At the end of the test section, a sloping broad crested weir is mounted to generate super-critical conditions at its crest, preventing free surface perturbations from reflecting back into the test section (Liao, 2004).

The experimental imaging area was located 10 meters downstream of the flume entrance. The camera was mounted on the ceiling of the laboratory facility, 2.8 meters above the water surface. This was the maximum separation distance achievable, therefore limiting the image area due to a fixed camera lens angle of 25^{o}. Care was taken to align the camera at 90^{o} with respect to the water surface and to align the image area at 90^{o} with respect to the mean downstream flow direction. The image area begins at the air/water/flume interface and extends into the center of the flume 1.32 meters, while reaching 1.07 meters in the streamwise direction.

2.2 Infrared Image Collection

Due to the nature of infrared thermography, environmental reflection can significantly contaminate the true STP of the object being imaged. At the given flow rate and depth, the surface of the water in the wide flume appears rather unperturbed to the naked eye. Surface deformations are minor and light is therefore somewhat clearly reflected. Depending on the angle, wavelength and intensity of external light sources (among other things), they may appear as extra noise over the image sequence. Although thermal reflections from the natural environment are unavoidable in a field setting, Garbe et al. propose a temporal gradient method in which image areas that are contaminated with environmental reflections are identified and de-weighted during image processing.

For most of the data sets collected in this thesis, this potential noise source was avoided by imaging at night with all laboratory lights turned off. Garbe's reflection de-weighting technique was therefore not used here, although it may prove to be valuable in the analysis of future field data.

2.2.1 Thermally Equilibrated Flow

In order to test the limits of this proposed velocimetry method, Data Set 1 was taken under the "worst case" flow conditions. As mentioned previously, due to the very smooth flume walls and the relatively slow flow velocities, the level of turbulence in the water is much lower than that typically expected to be found in the natural environment. Additionally, the water was allowed to approach thermal equilibrium with the experimental surroundings for several hours prior to collecting the first data set. With the weaker turbulence carrying fewer and smaller random parcels of water to the surface and such little temperature difference between the air and water, these two conditions combine to create a narrow temperature distribution on the water surface and therefore minimize the STP captured by the infrared camera. Data Set 2 was collected under the exact same conditions, but the laboratory lights were turned on.

Initial analysis of these "worst case" flow conditions with early versions of the displacement algorithms raised concerns that the fixed noise level of this specific camera would obfuscate such a weak signal (Figure 2), making image displacement analysis a fruitless effort. Images taken on water surfaces of similarly uniform temperature by superior infrared cameras (such as the one used in the Garbe study) clearly show a more coherent STP that is expected to provide much better velocimetry results. Since a camera of this caliber was unavailable for these particular experiments and ultimately the desire is to work exclusively with low-cost infrared cameras, the decision was made to physically alter the surface temperature of the flow to obtain an equally clear STP. This will significantly enhance the SNR similar to the manner in which traditional PIV technicians seed the flow with particles and artificially illuminate them.

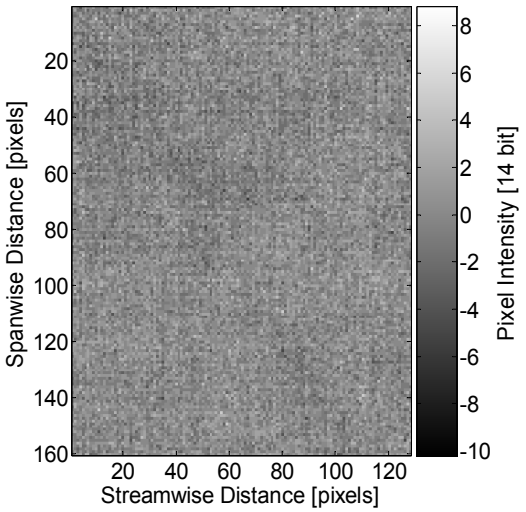

Figure 2: Thermal image (median background removed – see Figure 4 (a) for typical median background image) recorded under "worst case" conditions in which very little thermal diversity exists on the water surface. Flow is from left to right.

2.2.2 Thermally Disequilibrated Flow

In order to achieve the maximum temperature differential on the flowing water surface while disrupting the surface flow pattern as little as possible, several thermal "tagging" methods were tested. This can be accomplished by either cooling or heating different regions of the flowing water and ensuring that the maximum surface temperature differential is achieved in the imaging area. Ideally a non-contact method is desired in which parcels of water are heated or cooled remotely and therefore no physical obstruction to the water flow is required. This can be achieved using refrigeration coils at or near the surface or heating coils from beneath the flume. Using the refrigeration coil method would allow for a uniform or patterned cooling of the water surface some distance upstream, ultimately allowing the ensuing convective currents to take place, and drastically diversifying the temperature range on the water

surface. Similarly a submerged parcel of water that is heated upstream will induce the reverse convective currents to achieve the same goal. A third alternative exists to thermally tag the surface anisotropically with a heat source. This buoyant, heated water will advect downstream, maintaining some form of the imposed structure and appear as a strong STP in the infrared against the background of the cooler surface water.

Unfortunately, the resources available for this experiment were limited to methods that required the introduction of some physical interference with the existing flow. The first attempt at thermal tagging was to create convective currents by taking advantage of the temperature difference between ice and the room temperature water (roughly 25 ^{o}C). A mesh bag filled with roughly 100 kg of crushed ice was affixed along the entire width of the flume upstream of the imaging area. In concept, the water would flow through the mesh and be cooled as it slowly melted the ice, eventually sinking as it grew denser. Aside from being exceptionally impractical and difficult to implement, this method failed simply because the ice melted too quickly and the mesh bag proved too significant of a disturbance to the surface flow velocities.

Lacking the facilities to build a reliable non-contact method to cool the surface or heat the subsurface as was accomplished by Mosyak and Hetsroni, 2004, the only practical alternative was to introduce parcels of buoyant hot water upstream. This was accomplished with a simple garden hose flowing with hot water. The hose was fitted with a sprinkler attachment and sprayed evenly on the flowing water surface at several distances upstream. Data Sets 3 and 4 were collected in this manner (Figure 3). This produced a visible pattern in the thermal images, although the evenness of the distribution and fineness of the water droplets seemed to diminish the desired effect of creating a wide thermal diversification. For this reason, the sprinkler head was removed and the hot water was allowed to flow in bulk through the end of the hose

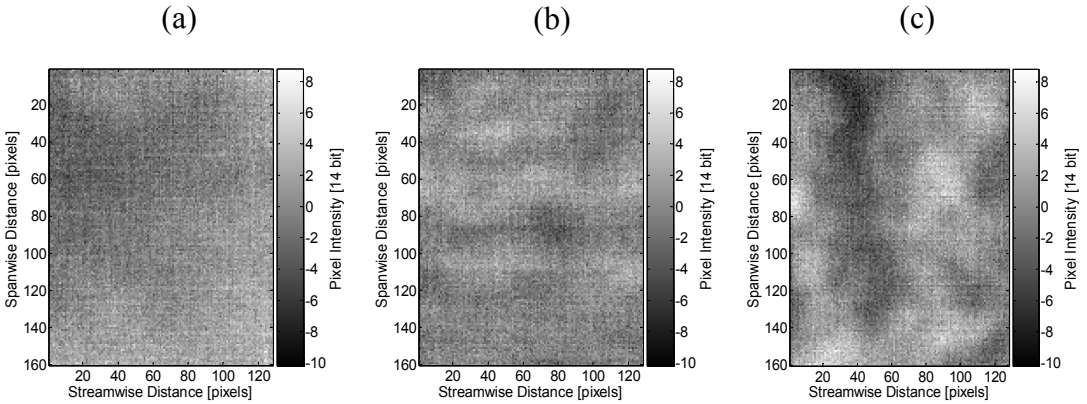

Figure 3: Thermal images (median background removed – see Figure 4 (a) for typical median background image) from Data Sets (a) 3, (b) 4, and (c) 5, respectively representing increasing thermal surface diversity. Flow is from left to right.

while it was manually moved back and forth across the flume. This method created more discrete and thermally visible hot parcels of water advecting downstream against the background of the cool surface water and therefore created the desired STP. Data Set 5 was collected in this manner. A comprehensive description of each data set is presented in Table 1.

Table 1: Data Set Characteristics

Data Set	Thermal Tagging	Tagging Distance Upstream	Lights	Sample Frequency	# Images
1	None	N/A	off	30 Hz	10,000
2	None	N/A	on	30 Hz	10,000
3	Spray	5 m	off	30 Hz	10,000
4	Spray	1.5 m	off	30 Hz	10,000
5	Bulk	1.5 m	off	30 Hz	10,000

2.3 Velocity Verification

In order to establish a control for this experiment, velocity measurements made at the water surface by another piece of velocimetry equipment are desired for comparison. Ideally these measurements can be made in the imaging area laterally across the surface simultaneously with the collection of the infrared images. For this experiment, a Nortek Vector ADV was used to obtain point measurements near the surface. This instrument consisted of a 15 cm probe attached to a 2 m cabled head that was mounted in an upwards facing position. Due to the limitation of having only one ADV available, measuring the surface velocity profile simultaneously with collecting images was not feasible. A single point measurement was made during data collection directly downstream of the imaging area. This was observed as a rough measurement of the change in surface water velocity due to the individual seeding methods that were employed in each set. Immediately following the collection of all five of the data sets, a surface velocity profile was recorded in the imaging area at an interval of 10 cm under the same exact conditions. Data was sampled at 16 Hz for approximately 60 seconds at each location.

2.4 Camera

The water surface area of interest was imaged using an FLIR Systems (formerly Indigo Systems) Omega 160 × 128 pixel infrared camera. The camera is capable of up to 30 frames per second frame transfer, has both 8 bit (256) and 14 bit (16384) dynamic range modes and a noise-equivalent delta temperature (NEdT) of < 80 mK. A bootstrap uncertainty interval analysis reveals that the typical pixel intensity 95% confidence interval is +/- 0.12 counts. It is unique in its field as it is

drastically less expensive (O($10K) vs. O($100K)) than other infrared cameras of comparable size and resolution. This is made possible by the distinct difference in technologies between the expensive and inexpensive infrared cameras. While traditional, scientific-grade infrared cameras physically count each individual photon that passes through the filtered lens, ultimately relating the number of photons per frame to pixel intensity, the inexpensive cameras correlate a bolometric measurement (i.e. the radiation-induced change in electrical resistance) to pixel intensities.

The software that comes packaged with the camera provides adequate control over many camera functions such as the automatic flat field correction and video output modes. Unfortunately, the software is deficient in the areas of file management and timing control, resulting in an unacceptable limit on total number of captured images and unpredictable frame drops and repeats. For these reasons Boulder Imaging of Boulder, Colorado was employed to adapt their Vision Now software to control the camera and compensate for these problems.

The camera is driven and controlled using an IBM Thinkpad T40 laptop equipped with a 1.50 GHz Intel Pentium Processor and 512 MB of RAM. Images are captured by the camera and transferred via IEEE 1394 (FireWire) to an external LaCie portable hard drive. This system was chosen to maximize performance and portability to facilitate use in both laboratory and field environments. The Vision Now software allows for live images to be viewed during data collection. Additionally, live images may be viewed directly from the FireWire module via an analog output.

The camera lens is fixed with a focal length of 18 mm and a viewing angle of 25°. This narrow angle lens creates the problem of requiring a high overhead clearing above the water surface that is to be imaged. This issue may be easily overcome in the future because FLIR Systems now manufactures various other commercial lenses including a wide angle 8.5 mm lens with a viewing angle of 55º. The image size was

calibrated by physically probing the edges of the image area with a heated rod and measuring the two dimensions of the image area with a measuring tape. It should be noted that much of the research involved with thermography of flowing water surfaces has been accomplished using high resolution infrared cameras with very low NEdTs. This allows the researchers to view extremely fine thermal structure in an environment that is naturally quite uniform in temperature. A survey of several related papers regarding gas transfer at the air water interface reveals typical surface water temperature distributions have a total dynamic range of less than 200 mK. Many of the infrared cameras used in these research efforts are able to resolve this temperature difference into a dynamic range of 30 counts (a resolution of less than 10 mK). The Omega camera used for the research in this paper is only able to resolve a temperature difference of that magnitude into three to four counts. Since the goal of this velocimetry technique is to be a widely used and distributed large-scale river velocimetry device, the need for an extremely expensive camera would likely render this method impractical. For this reason, one of the long-term focuses of this research is to determine the minimum camera specifications that will be required to reliably obtain velocity profile results from a flowing river surface.

CHAPTER 3

EXTRACTING SURFACE VELOCITY PROFILES FROM QUANTITATIVE THERMAL IMAGE SIMULATIONS

This thesis is an investigation into the effectiveness of analyzing sequential infrared images of a flowing water surface with QI displacement algorithms to extract the surface velocity profile. In chapter 4 the results of this analysis are presented and discussed, and in some cases compared to measurements made by the ADV. Before discussing these results, however, it is essential to understand some of the challenges that analyzing infrared images with displacement algorithms present. Additionally, the effectiveness of different types of algorithms and methods are quantified and compared in this chapter by using Monte Carlo Simulations.

3.1 Background

Traditionally, QI (more specifically, PIV) has been used to obtain a comprehensive picture of fluid flow velocities in a small scale environment. This usually involves seeding of the flow in some manner and often requires external illumination by a light source (e.g. a laser light sheet). The resulting images of discrete illuminated particles are processed through a correlation algorithm which determines a mean displacement value for each region of the image and associated group of particles (and therefore, each parcel of fluid, it is assumed).

While the concept of using a correlation algorithm to compare two sequential infrared images seems quite similar to traditional PIV, there are several distinct and important differences. Primarily, as is noted in the SIV research, these images lack the

discrete particles and instead contain the signature of the unevenly dispersed scalar tracer (in this case, temperature). Given an adequate thermal diversity at the air-water interface, this may create a STP in the infrared image that can be visually traced as it advects. Although the continuity of the scalar image may open the door to alternative analytical methods that take advantage of the physics of fluid motion (such as SIV), the rather high SNR that is required to achieve accurate first and second order differentiation of the intensity field that are crucial to these methods is impractical for the thermographic instrumentation available to this thesis. Therefore, this chapter will

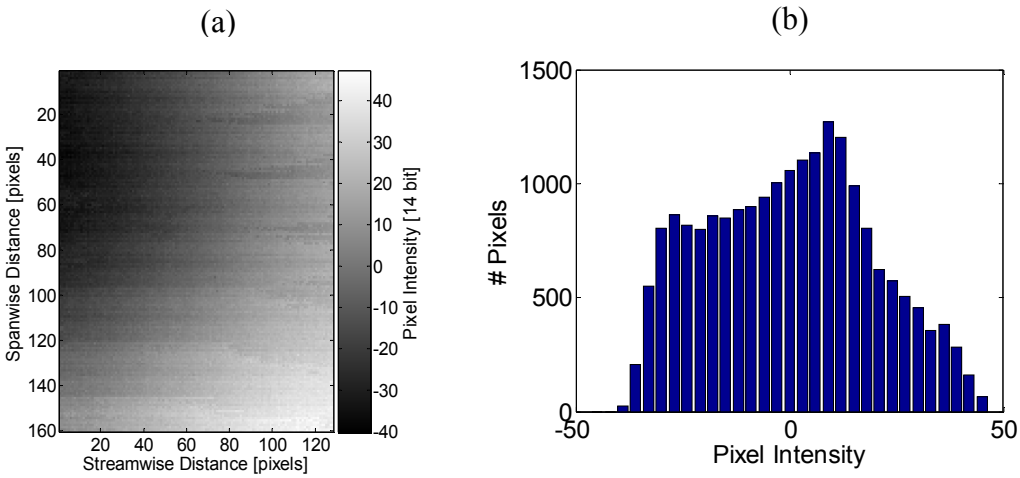

Figure 4: (a) Typical median background image normalized to a mean pixel intensity of zero; (b) Intensity histogram of background image (a)

establish that a displacement algorithm that is capable of accurately tracking STPs must be carefully chosen to maximize the effectiveness of this velocimetry method.

Secondly, due to the tendency of the flowing water surface to have an exceptionally narrow temperature distribution, the signal that is being studied is extremely weak. As with any camera, this particular infrared camera has an intrinsic non-uniform background image intensity and a set level of background noise (Figure

4). In many of the environments that were imaged, the extremely weak signal was often obscured by the background image intensity and/or the background noise level. In other words, the dynamic range of the background can easily be several times larger than the expected dynamic range of the signal that is being monitored on both the subwindow scale and the scale of the entire image (Figure 5). The displacement algorithm presented in this chapter is optimized to extract a surface velocity profile

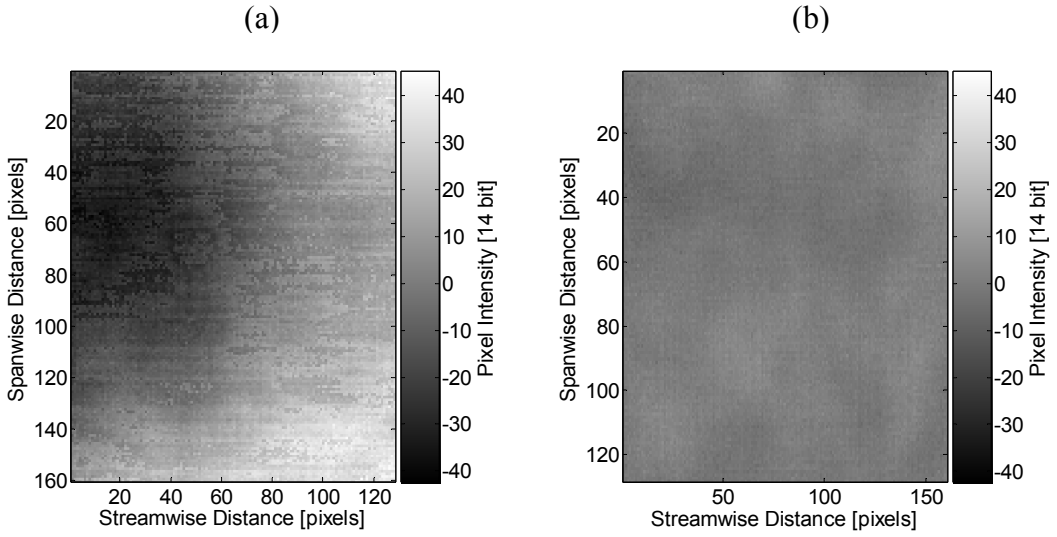

Figure 5: (a) Image from Data Set 5; (b)The same image with the median data set image removed (*Note:* This is the same image as Figure 3 (c) with different scaling)

from images with a very low SNR.

Lastly, the fluctuation of image pixel intensities over time and space will be of significant concern. Spatial background intensity fluctuations will adversely affect the performance of displacement algorithms, specifically in low SNR images. As is discussed in Chapter 4, the necessary step of background image removal will highlight any temporal changes in the background intensity pattern, and will ultimately force the displacement algorithm to return a strong tendency to zero-displacement.

Additionally, rapid thermal diffusion of the STP during its short time on the surface of the water will cause a potentially significant distortion of the pattern that is being tracked. This pattern distortion reduces the overall effectiveness of the displacement algorithms. This latter issue can be controlled by the amount of time that is allowed to pass between surface recordings.

3.2 Monte Carlo Simulation Images

In order to quantitatively test different displacement algorithms and properly design proposed laboratory and field experiments, a Monte Carlo Simulation image generator was developed. The goal of this simplistic model was to produce grayscale images that resemble a thermographic scalar field in flow. For simplicity's sake, the generator does not model fluid physics. Similar synthetic images that are based on the physics of surface renewal, thermal diffusion, and surface temperature distribution have been developed (Handler et al., 2001); however, that level of detail was not necessary to carry out the desired comparison of the displacement algorithms in this thesis. Instead, this generator randomly superimposes several deformed, skewed, and rotated two-dimensional Gaussian intensity distributions over a blank image. The distributions of the density and scale of these random shapes were set as variables, allowing the image to represent the near field or far field. Images were generated on a trial and error basis while the variables were adjusted until they closely resembled preliminary thermographic images that were recorded in the laboratory. The images were then digitally translated using a two sided boundary layer flow modeled with the $1/7^{th}$ power law. No-slip boundary conditions were established at the flume walls (the 128 pixel edges of the image) and the images were translated a maximum of 10 pixels per frame pair in the direction perpendicular to these edges.

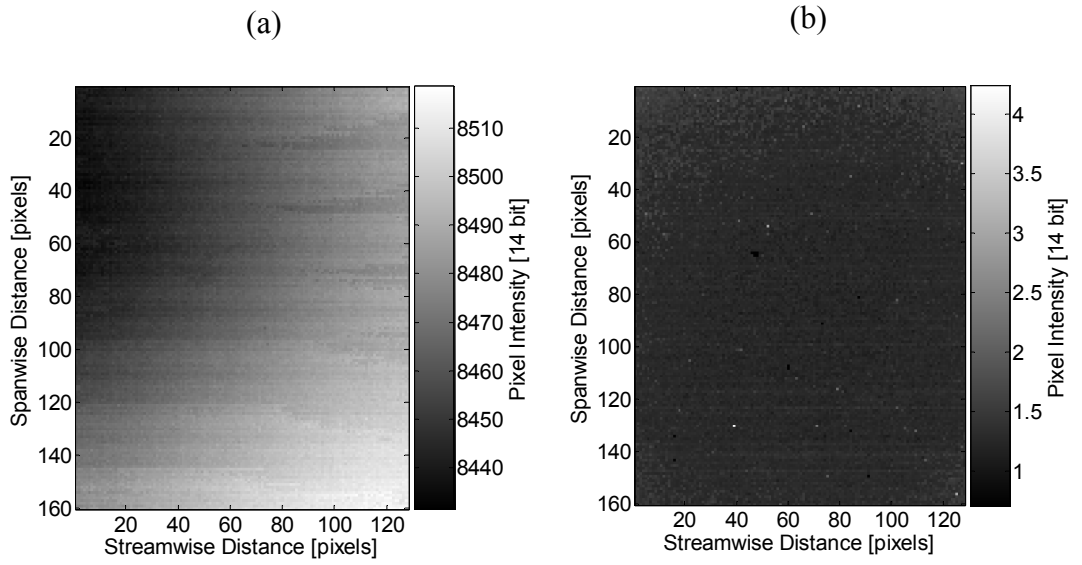

Figure 7: (a) Mean temporal camera pixel intensity; (b) Root mean square temporal camera pixel intensity

The camera noise was modeled by using a direct measurement from the Omega camera itself. A uniform temperature blackbody was not available for a precise background image measurement. Instead, the camera was left to equilibrate at room temperature with the lens cap on and a series of images was captured under these conditions. The time series was de-trended, the overall camera noise was calculated as

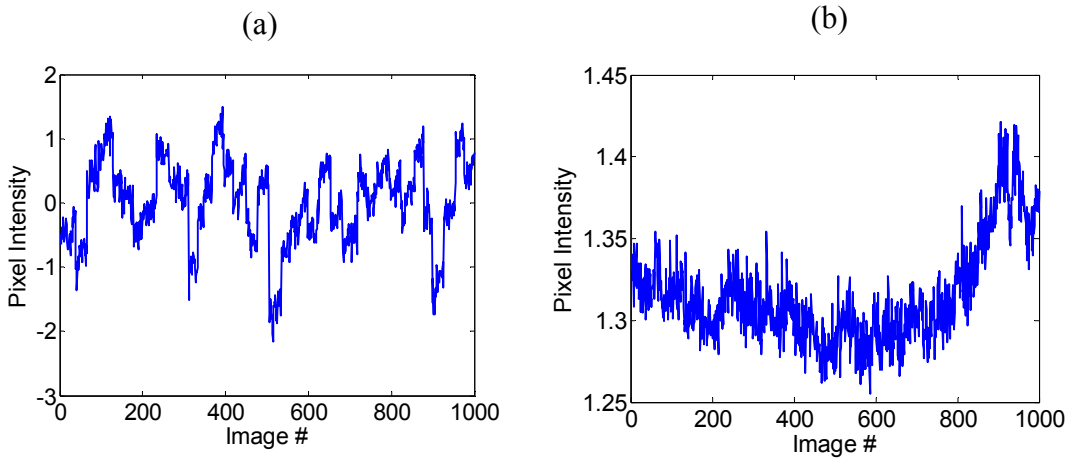

Figure 6: (a) Detrended mean spatial pixel intensity; (b) root mean square spatial deviation from the detrended pixel intensity (background image removed)

the average root mean square deviation in time at each pixel (found to be 1.3 counts) and the median background image was recorded (Figures 6 and 7). The amplitude ratio of noise to background image is modeled to match this specific camera's and the signal amplitude can be modified to represent any range of temperature distributions passing through the field of view.

A data set of 2000 images (1000 pairs) of noiseless signal was created to act as a foundation for image Sets A and B. These data sets were then created by varying the Monte Carlo Simulation signal-to-noise ratio (denoted as SNR_{MC}: the ratio of the root mean square signal amplitude to the root mean square noise amplitude) to represent the span of expected thermal environments and varying thermal resolution of different imaging systems. Due to the thermal resolution limitations presented by using the Omega Camera, the Monte Carlo Simulation data sets will focus on simulating very low SNR sampling environments. The two data sets that were created (Table 2, Figure 8) were chosen to investigate (A) the scenario in which the signal strength is much greater than the maximum spatial difference in background intensity due to the inherent camera characteristics, and (B) the opposite scenario in which the signal strength is much weaker than the maximum spatial difference in background intensity. Each displacement algorithm will be used to analyze the simulated data sets. Despite not modeling the turbulent surface hydrodynamics, these Monte Carlo Simulations will provide quality insight in comparing how well each algorithm responds to tracking the STP in a low SNR environment, and identifying the minimum SNR_{MC} value at which the algorithm fails to calculate the proper velocities.

Table 2: Monte Carlo Image sets A and B are identical, except for the addition of the inherent background image of the Omega Camera in Set B

Group #	# of Images	SNR_{MC}	Noise Strength	Background Strength (Set A)	Background Strength (Set B)
1	2000	0.05	1.3	0	1
2	2000	0.10	1.3	0	1
3	2000	0.15	1.3	0	1
4	2000	0.20	1.3	0	1
5	2000	0.25	1.3	0	1
6	2000	0.30	1.3	0	1
7	2000	0.35	1.3	0	1
8	2000	0.40	1.3	0	1
9	2000	0.60	1.3	0	1
10	2000	0.80	1.3	0	1
11	2000	1.00	1.3	0	1
12	2000	1.20	1.3	0	1
13	2000	1.40	1.3	0	1
14	2000	1.60	1.3	0	1
15	2000	1.80	1.3	0	1
16	2000	2.00	1.3	0	1
17	2000	2.20	1.3	0	1
18	2000	2.40	1.3	0	1
19	2000	2.60	1.3	0	1
20	2000	2.80	1.3	0	1
21	2000	3.00	1.3	0	1

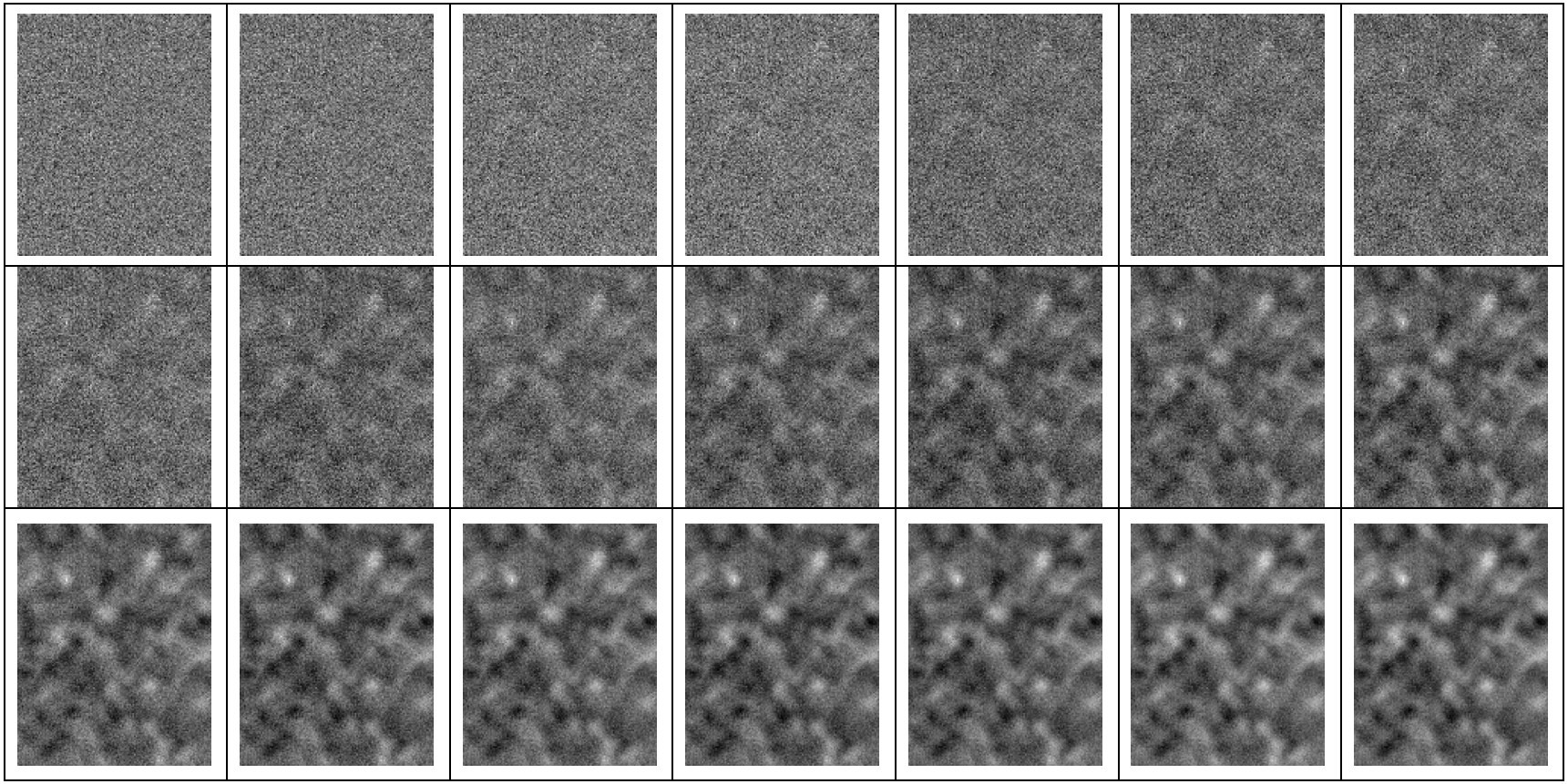

Figure 8: Monte Carlo Simulated images (See Table 2 for SNR_{MC} values): Groups 1-7 (top row); Groups 8-14 (middle row); Groups 15-21 (bottom row)

3.3 Traditional PIV Analysis

The PIV software developed by Cowen and Monismith (1997) (along with all of its subsequent upgrades) provided the foundation on which all further QI codes discussed in this paper were developed. The original version of this algorithm was intended for use with traditional PIV images. It utilizes a Fast Fourier Transform (FFT) correlation algorithm and implements several enhancing features such as, image convolution, subwindow overlap, multiple filters, and data smoothing. The user is given the flexibility to choose subwindow sizes of $2^n \times 2^n$ pixels, and therefore has significant control over the resolution and accuracy. A significant amount of research has been accomplished on this PIV method, identifying details such as the optimum particle size, dynamic range and concentration of particles in each subwindow. While this version is a proven and robust tool in analyzing traditional PIV images, it is yet to be seen how effective a tool it is for thermographic image analysis.

In order to obtain an understanding of how Cowen's PIV method will perform on thermographic images, it is helpful to compare the analysis of traditional synthetic PIV images with the analysis of the similarly translated Monte Carlo Simulation images (denoted MC Set 1 for the purposes of this thesis) discussed in the previous section. To make a fair comparison, both sets of 1000 images have a high SNR_{MC}, are of equal size (Figure 9) and are subjected to a two-sided boundary layer downstream translation (*Note:* This translation pattern is used for all synthetic images in this thesis). The thermographic simulated images for MC Set 1 are taken from image Set A, Group 21, as presented in Table 2. The traditional PIV images are created from Cowen's image generator (Cowen & Monismith, 1997), with a mean background noise intensity set to 50 counts (on an 8-bit scale), maximum particle intensity set to 250, particle density of 20 particles per subwindow, and the standard deviation of

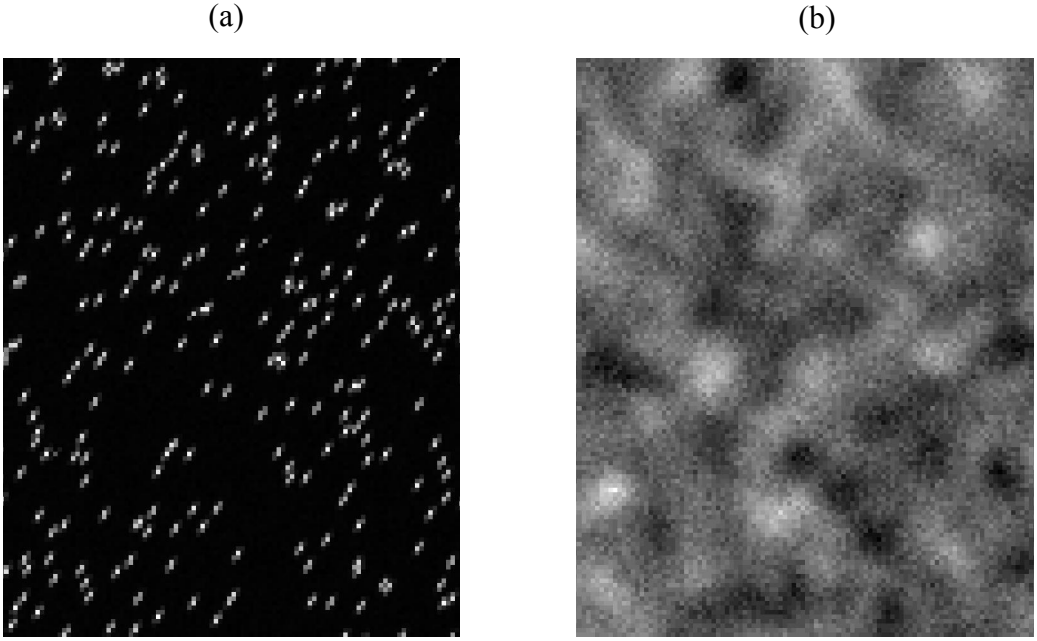

Figure 9: (a) Simulated traditional PIV image (maximum particle intensity: 250; background noise: 50); (b) Simulated infrared image ($SNR_{MC} = 3.0$)

particle diameter set to 0.5 pixels. The subwindow size is set to $N = 32$ pixels square and no camera background effects are added. The images were analyzed by the same algorithm and no added features such as the Gaussian filter or image convolution were used.

Cowen's PIV algorithm performs quite well on the original simulated PIV images (Figure 10). The tendency of this algorithm to slightly underestimate the magnitude of translation is well known and has been addressed by the development of enhanced features that are beyond the scope of this thesis. The translation results plotted on the same graph suggest that the algorithm performs satisfactorily on the simulated thermographic images as well. A closer look, however, reveals that the percentage of valid vectors (those remaining after the post-processing takes place) drops drastically, while the root mean square deviation from the mean translation

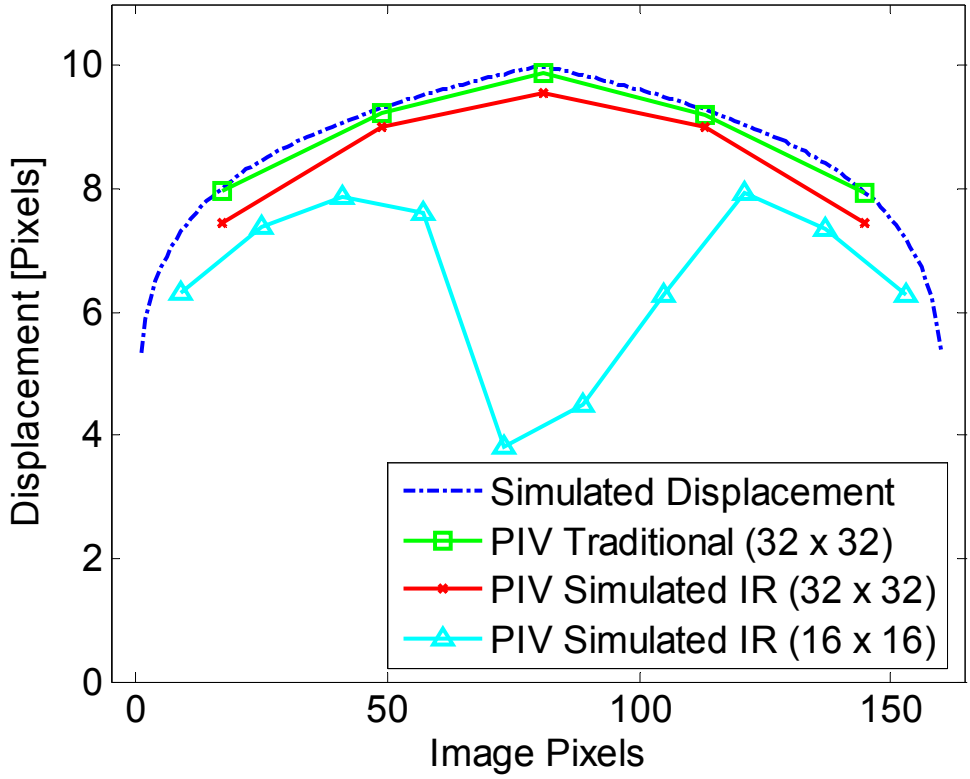

Figure 10: Cowen's PIV algorithm results

vector increases (Table 3). This alone hints at the possibility that this algorithm is not entirely appropriate for use with these image types.

Furthermore, due to the large size of the subwindow selection relative to the total image size, the level of resolution leaves much to be desired, resulting in just five independent data points across the entire image. For this reason, the subwindow size was reduced to 16 × 16 and the PIV algorithm was again run on MC Set 1. As expected when reducing the subwindow size, the percentage of valid vectors decreased and the root mean square deviation increased significantly due to the reduction in available data to analyze. Unfortunately, the algorithm was unable to

accurately produce a displacement profile that resembled the one actually imposed on the images (Figure 10).

Table 3: **Table 3**: Cowen's PIV algorithm statistics

Image Set	RMS Error [%]	σ [pixels]	Valid Vectors [%]
Traditional	0.7	.08	97
IR (32 × 32)	4.8	.47	80
IR (16 × 16)	29.3	3.1	58

3.4 Displacement Algorithm Improvements

3.4.1 Subwindow Extension

The simple test presented above suggests that, given the proper amount of data in the subwindow, this algorithm is able to produce a number of valid displacement vectors that will reasonably approximate the actual displacement field. With this in mind, a small adjustment to Cowen's algorithm can be made to not only maximize the amount of data in each subwindow, but also maximize the resolution in one direction at the expense of resolution in the other. While traditional PIV technicians are typically interested in whole field flows with resolution equally important in both the x and y directions, we intend on taking advantage of the fact that the bulk of the fluid flow will take place primarily in one direction (chosen in this thesis to be the positive x-direction). Therefore to achieve maximum signal in the subwindows, while still maintaining a large degree of resolution in the y-direction, each subwindow is extended in the streamwise direction and compressed in the lateral direction. While

the result of this alteration will severely limit the use of this version to unidirectional flow in the *x*-direction, the increase in signal is necessary to make it a robust tool in analyzing these infrared images. For the purposes of this thesis only, this version of the algorithm will be called "PIV-ext."

PIV-ext uses the same correlation algorithm as Cowen's original code, but simply allows for rectangular subwindows instead of requiring square ones. The lengths of these subwindows are still constrained (by the nature of the FFT currently in use) to be of length 2^n pixels (*Note:* This may be easily relaxed at the expense of a moderate increase in computational time). Test runs quickly indicated that the maximum resolution while maintaining acceptable accuracy was obtained by using subwindows of size 8 × 64 pixels. For the Omega camera image resolution, this allows for a maximum of 19 measured velocities laterally across the image area. .

In order to fairly evaluate the effectiveness of this minor alteration, PIV-ext was used to analyze MC Set 1 also. The results (Figure 11) reveal the success of this minor alteration as the error is drastically reduced, the resolution is nearly quadrupled, and the number of valid vectors increases. While these results are very promising compared with the results of the previous version's analysis of the same images, they do not compete quite as well with the analysis of the traditional PIV images. Additionally, due to the nature of the subwindow size constraints mentioned above, this algorithm requires that nearly half of the image data be disregarded. To achieve success in a low SNR environment, clearly as much data as possible must be analyzed, and therefore further algorithm options are investigated.

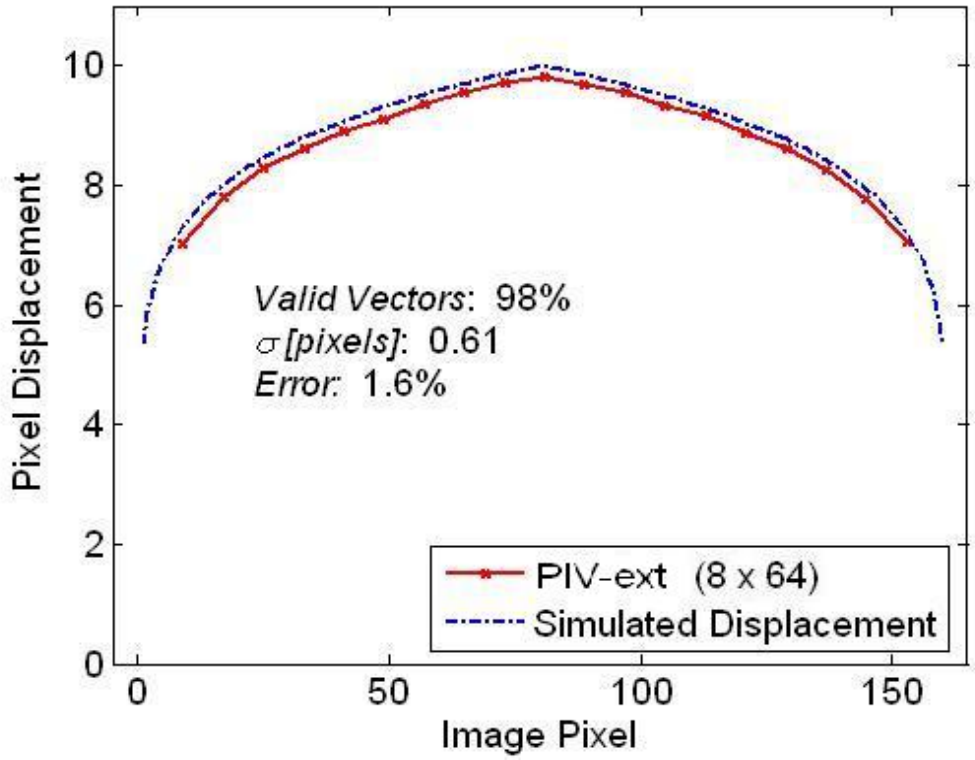

Figure 11: PIV-ext results for MC Set 1

3.4.2 MQD Integration

Hetsroni et al. (2001) noted in their analysis of similar thermographic images of an advecting heated pattern that the traditional PIV algorithm they used did not provide adequate accuracy for their purposes. They therefore chose to compare their PIV results to the results of the computationally expensive Optical Flow algorithm, which is designed to recognize and track image features. This technique proved to be a bit more effective despite the computation time and therefore leads us to another alteration of this PIV code that can be made in order to increase its robustness in this new infrared environment.

Gui and Merzkitch (2000) presented the Minimum Quadratic Difference (MQD) algorithm (a least-squared algorithm that, in principle, tracks patterns rather than individual particles) in an effort to better determine displacement in traditional PIV images that have non-uniform seeding distribution or non-uniform background illumination. They successfully demonstrated this technique by comparing their algorithm to several traditional PIV methods and ultimately showed that the MQD method was more accurate and much less susceptible to varying particle density and size distribution. Since our images do not have individual particles, instead having only a distinct STP advecting downstream, an algorithm that is robust to large changes in these two variables could potentially perform much better than the traditional correlation based method.

PIV-ext was adapted to incorporate the MQD method, thereby creating a new displacement algorithm version which will be referred to as "MQD-ext" for the remainder of this thesis. Keeping in mind the goals of using the maximum data available and obtaining fine resolution in the y-direction, the window extension concept was implemented in this algorithm as well. Due to the small size of these images and the speed of the computer system involved, computation time was not an issue and Gui and Merzkirch's acceleration methods were not employed.

Figure 12 provides a graphical layout of the implemented subwindow structure. A long subwindow (*F*) is identified in image one, and the algorithm is allowed to sequentially compare it to a finite number of potential displacement locations in image two (*G*). The least-squared difference between the two subwindows is calculated for each potential location and recorded in the resulting displacement plane (*H*). The minimum value of *H* represents the resulting displacement for the original subwindow and a subpixel fit is accomplished by using a Gaussian interpolation estimating function. One significant difference that results

from the use of this algorithm over the original correlation algorithm with an FFT is that the subwindow data is not assumed to be periodic. While this significantly diminishes the advantage gained by the central-difference dynamic subwindows method used in PIV-ext, it also eliminates the ability to evaluate the subpixel fit when the resulting displacement is found to be on the boundary of *H*. For this reason, displacement values are ignored on the boundary of *H* and these MQD values are instead used *only* for subpixel fit interpolation for their inward adjacent MQD values.

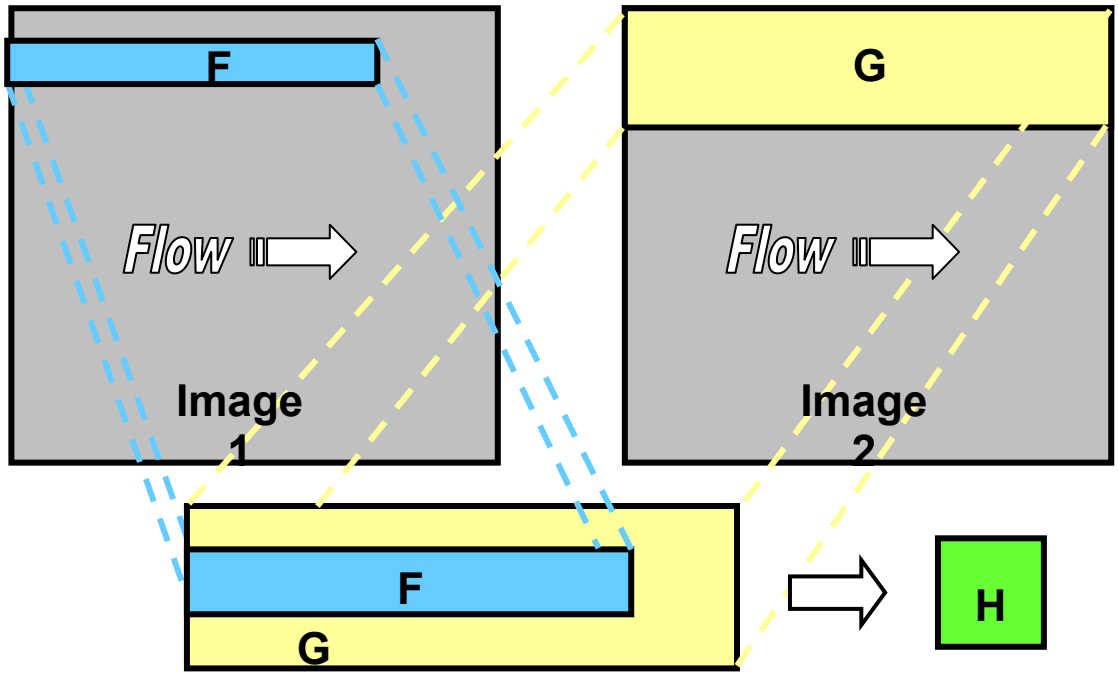

Figure 12: MQD-ext subwindow search scheme

To illustrate this, consider the arbitrary MQD peak height *H(i,j)* in the plane *H(m,n)*. Although MQD values are calculated for all $i < m$ and $j < n$, only the values located at $2 \leq i \leq m$ -1 and $2 \leq j \leq n$ -1 are used to search for MQD peak magnitude. In the case that the greatest peak magnitude is found to be at *H(i,n-1) and* the peak magnitude at *H(i,n)* happens to be greater than that, the Gaussian sub-pixel fit model fails, and the displacement vector is rejected. Otherwise, the boundary value is used to

appropriately approximate the sub-pixel fit. This issue, of course, can be controlled by the user in the experimental design (via limiting the time between images within a pair) and post-analysis design (by defining (*m,n*) such that all physically realizable displacements are contained within the usable portion of the plane.

MQD-ext was also used to analyze MC Set 1 and as predicted, the results are significantly better (Figure 13). The root mean square error is reduced almost to zero. While the valid vector count seems on the surface to have increased, it should be noted that this is partially a result of the non-iterative nature of this MQD algorithm. While the original code dynamically moves subwindows *F* and *G,* iteratively searching for the best fit and often returning spurious vectors when this method fails to converge or searches outside of the image area, the non-periodic nature of the implemented MQD algorithm provides little advantage to such a dynamic subwindow search, and hence only makes one pass per subwindow pair. Therefore, there are fewer opportunities for the algorithm to identify erroneous vectors. Furthermore, the *only* way in which MQD-ext will identify an erroneous vector is when the subpixel fit interpolation fails as described in the case above. The comparison of valid vector counts between PIV-ext and MQD-ext, therefore becomes somewhat misleading, as each algorithm currently rejects vectors by entirely different means (i.e. PIV-ext mostly from non-convergence, and MQD-ext entirely from subpixel fit failure) that are unique to the individual algorithm. It should also be noted that this inability to throw away spurious displacement vectors will ultimately lead to a greater root mean square deviation for all algorithms.

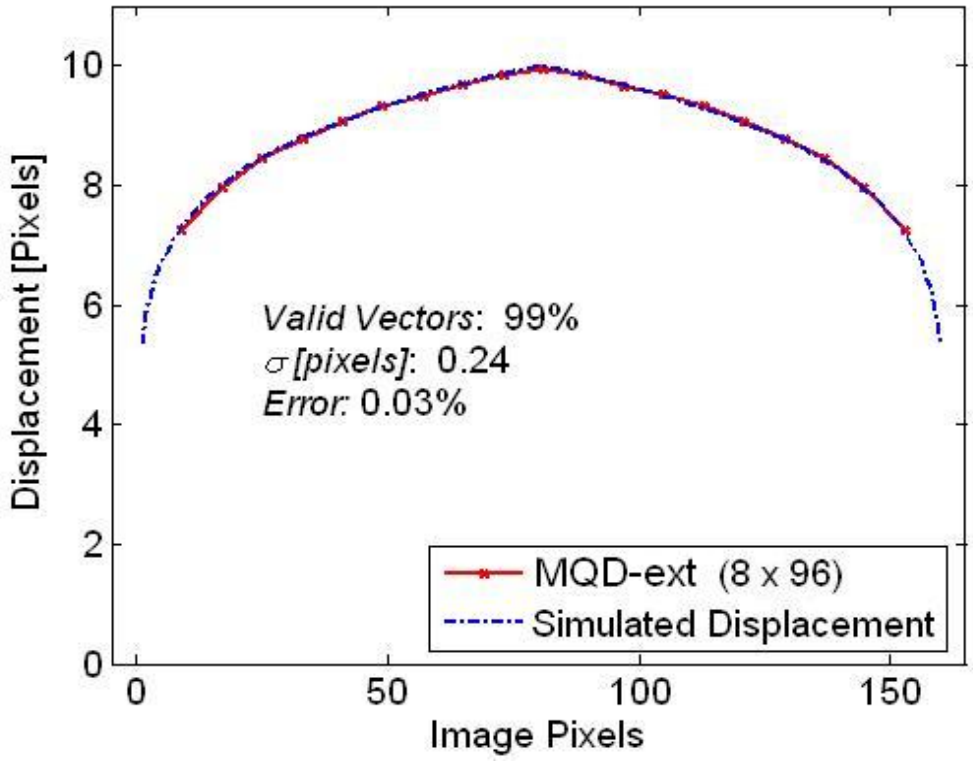

Figure 13: MQD-ext analysis of MC Set 1

3.4.3 CBC Integration

The results of the MQD-ext analysis on MC Set 1 are quite good and further algorithm investigation scarcely seems necessary. However, as has been stated earlier, one of the primary goals of this thesis is to establish that accurate displacement measurements are possible in an extremely low SNR environment. To further develop this algorithm to be robust in an environment such as this, one can implement the correlation based correction (CBC) method presented by Hart (2000). This method employs a multiplicative noise-canceling technique in which several slightly overlapping displacement planes from one local area of the image are multiplied on top of one another. Since the background noise is presumably random while the signal

is deterministic, the multiplication of overlapping planes leads to a reduction in noise generated peaks while preserving the signal generated peaks. The resulting displacement peak is expected to be much more pronounced on the CBC displacement plane than on any of the individual displacement planes.

To implement this technique, the MQD-ext code was altered to multiply the displacement planes resulting from six overlapping subwindows. This new displacement algorithm version is named "MQD-CBC". Three of the planes result from shifting the original subwindow location a finite distance in the positive and negative *y*-directions. The other three come from reducing the original subwindow length down by a third and shifting a finite distance in the positive *x*-direction only, repeating the *y*-directional shifts as well (Figure 14).

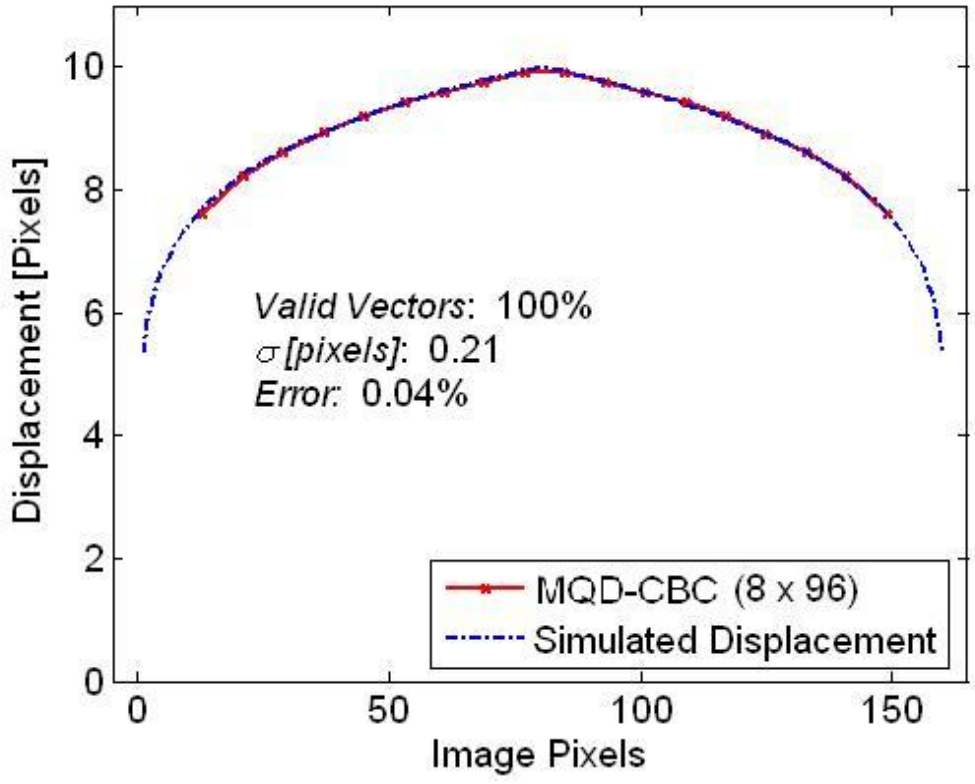

Figure 14: MQD-CBC analysis of MC Set 1

While these results from MQD-CBC (Figure 15) are nearly indistinguishable from the results from MQD-ext, further tests on images of much lower SNRs will shed light on this version's robustness.

3.4.4 Quantifying the Signal-to-Noise Ratio

It is expected that due to the nearly uniform temperature distributions on the flowing water surface and the high noise level of the Omega camera, determining displacements from these thermographic images with the various QI algorithms will be very difficult. In order to develop another potential comparison between these algorithms, it is convenient to create a method of quantifying the SNR. For the further purposes of this thesis, we will define the SNR as the ratio of maximum magnitude of the displacement plane peak to the median displacement plane value (*Note:* This is different from the definition of SNR_{MC}). In order to obtain this value for MQD-ext and MQD-CBC, the displacement plane is flipped upside down (as MQD searches for the displacement plane *minimum*). Furthermore, for MQD-ext and MQD-CBC, the edge peak magnitudes of the displacement plane will not be considered in SNR calculations. To make a fair comparison only a limited area (i.e. comparable displacement values to those resulting from the two MQD algorithms) of the much larger PIV-ext displacement plane is used for this SNR calculation.

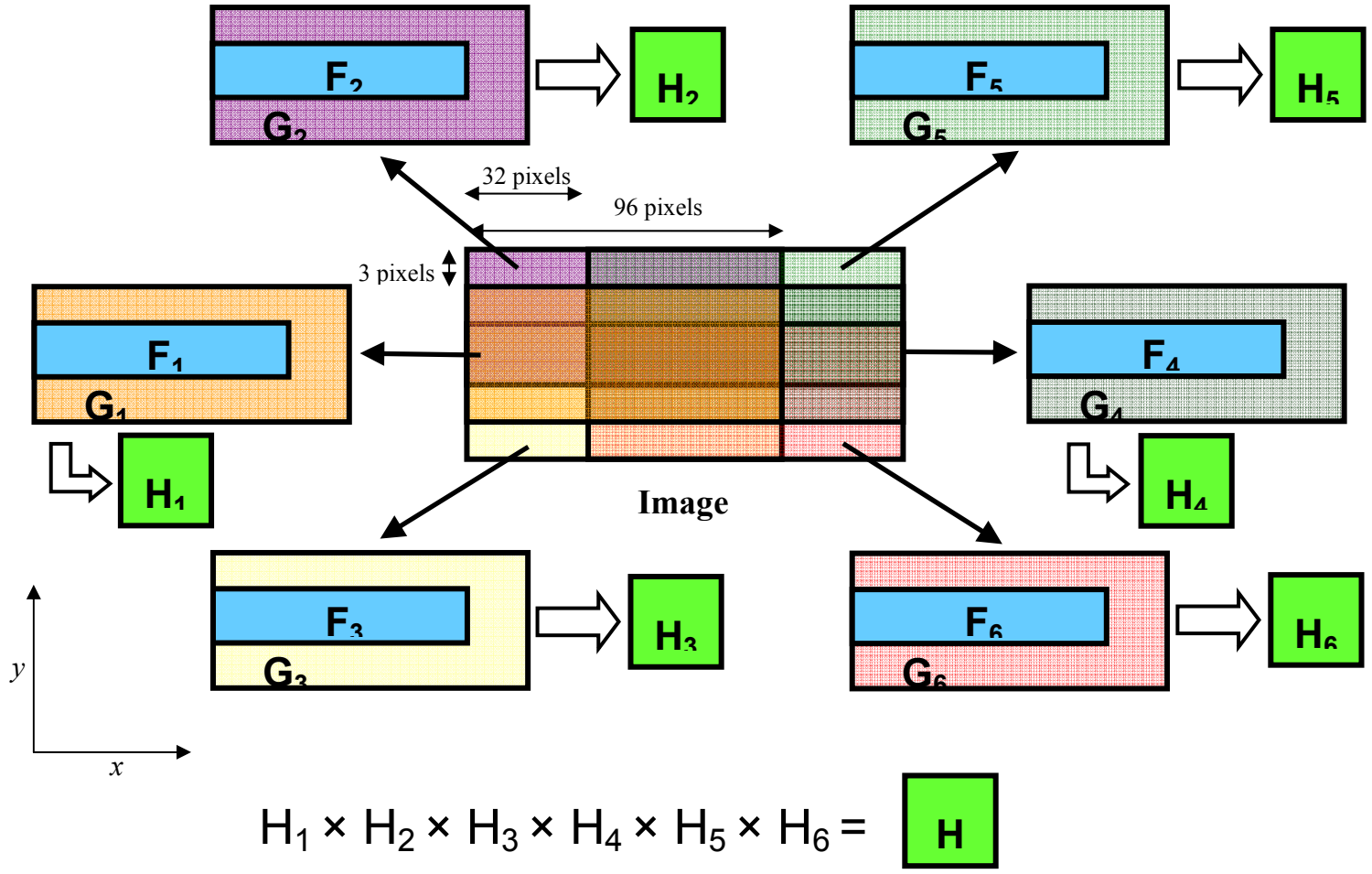

Figure 15: MQD-CBC multiplies several displacement planes from overlapping image areas.

3.5 Algorithm Comparison

With three displacement algorithms developed that each provide a respectable level of accuracy on the most basic simulated thermographic images, a detailed comparison can be accomplished by analyzing the previously discussed Monte Carlo Simulation image sets A and B. This analysis will shed light on how well each algorithm performs in a low SNR environment and reveal the effects of subtracting out a strong background intensity gradient. The results of this analysis will determine which algorithm will likely be best for use on the laboratory and field images to be analyzed in the future.

To analyze the 2,000 images in Set A, all of the input variables discussed above, such as subwindow sizes, were kept the same. Since Set A was created without the added obstacle of the simulated camera background intensity image, no median image background is calculated for removal during any PIV algorithm analysis. Additionally, to make a comparison somewhat more reasonable, post processing of the PIV-ext results was adjusted to only allow vectors that fall within expected displacement windows of MQD-ext and MQD-CBC (which is defined as -3 to 27 pixels in the *x*-direction and -3 to 3 pixels in the *y*-direction) and the adaptive Gaussian and local median filters were turned off. The results of PIV-ext, MQD-ext, and MQD-CBC on Image Set A are presented in Figure 16.

It becomes immediately obvious that none of these algorithms as they have been designed for the purposes of this thesis are effective at determining the overall displacement for images with weak STP. Not until the SNR_{MC} has reached a value of 0.4 does the error reduce to levels that are comparable to those seen in the analysis of MC Set 1. Not coincidentally, this signal strength value corresponds to the value at which the SNR begins to slightly increase, indicating that the signal is rising above the

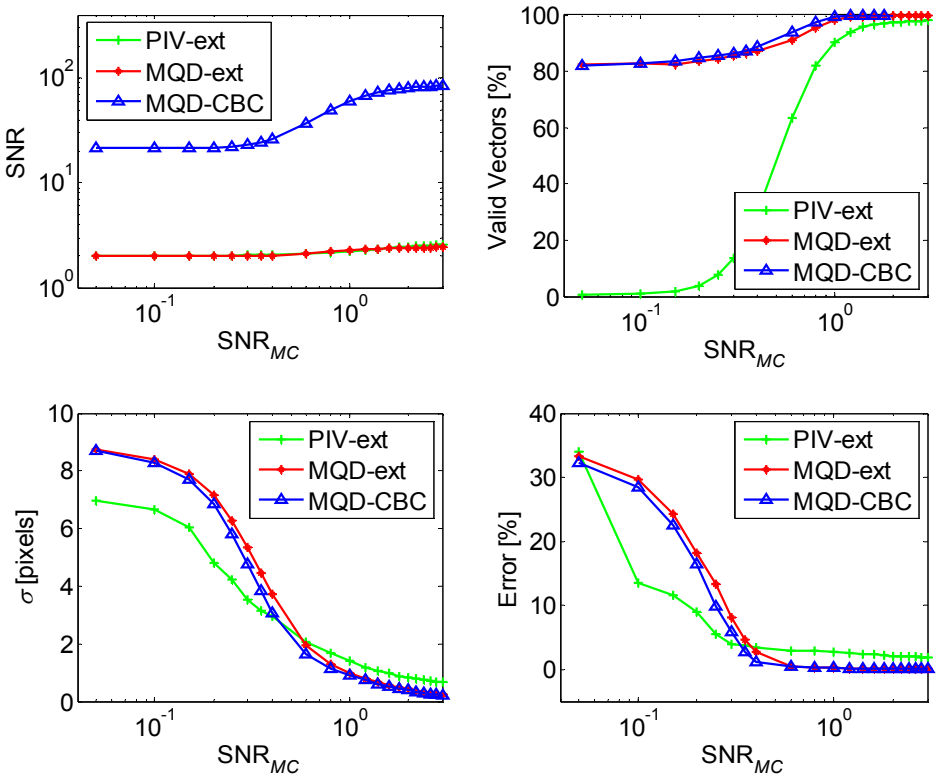

Figure 16: Displacement algorithm results for Image Set A

noise level often enough for the algorithm to distinguish it from the noise. At SNR_{MC} < 0.4, it should be noted that PIV-ext and MQD-ext SNR ≈ 2. These images are almost entirely noise and performing correlation or MQD on two different noisy arrays will simply produce a displacement plane that is equally noisy. As a result, the maximum displacement peak is often twice the magnitude of the median displacement value, as should be expected from a Gaussian distribution of noise on that plane. When these noisy displacement planes are multiplied together (as occurs in MQD-CBC), the noise is expected to cancel itself out, thereby amplifying the deterministic signal. This effect can clearly be seen as the SNR for MQD-CBC is much greater.

Initial observation of the error and standard deviation comparisons suggests that PIV-ext is the superior displacement tracking algorithm. However, further

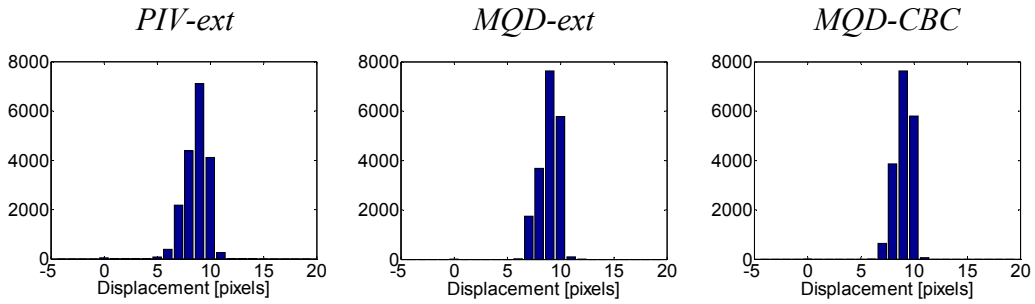

Figure 17: Displacement histograms for Group 21, Image Set A

investigation of the valid vector percentages provides a caveat before reaching this conclusion. As stated in the previous section, PIV-ext is an iterative correlation algorithm with an in-built mechanism to discard vectors that are unlikely to have resulted from a valid correlation. On top of this ability to eliminate spurious vectors, we artificially discarded vectors that did not fit into the prescribed displacement search area defined for algorithms MQD-ext and MQD-CBC. The results of these eliminations can be seen as the percentage of valid vectors is quite low for the regions in which PIV-ext seems to out-perform the other two algorithms.

Beyond the SNR_{MC} value of 0.4, the algorithms begin to behave as they did in the initial tests, with MQD-ext performing nearly equally as well as MQD-CBC, and both of them significantly outperforming PIV-ext. A clearer illustration of why this is occurring may be obtained by plotting the displacement histograms for valid vectors obtained from each subwindow in all three algorithms. In image groups that have SNR_{MC} much greater than 0.4 (Figure 17), MQD-CBC is producing the tightest distribution of displacement vectors around the proper value (10 pixels), while MQD-ext has a slightly higher standard deviation, and PIV-ext still higher yet. Note that the valid vector count for this example is nearly 100% for all three algorithms. On the

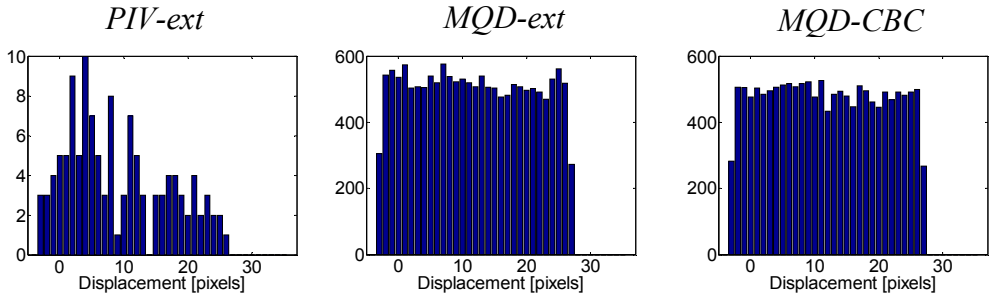

Figure 18: Displacement histograms for Group 01, Image Set A

other hand, when the SNR dips extremely low (Figure 18), MQD-ext and MQD-CBC produce what appears to be a uniform noise level across all possible displacements, while PIV-ext has discarded 99.4% of the resulting vectors, allowing only those with a higher probability of being actual displacement vectors to pass. Although it allows far fewer vectors, it seems that PIV-ext's iterative search algorithm eliminates much of the noise and apparently does a better job of estimating the total displacement at such low SNR_{MC} levels. However, none of the histograms produced by these three algorithms indicate that the proper signal has been successfully tracked. Although PIV-ext results in a lower overall error in the low SNR_{MC} image set, the peak of the displacement histogram is not located at the proper displacement value. The results that seem to indicate that this algorithm is more accurate at lower SNR values may be attributable to the nature of the noise pattern produced by the algorithm used in PIV-ext when it is used to evaluate randomly generated noise.

Despite the obvious superiority of the MQD-ext and MQD-CBC algorithms' abilities to estimate more accurate and precise displacements, the results of this single test suggest that the iterative method utilized by PIV-ext enables it to produce much better results in these simulated infrared images at very low SNR. With the possibility that this apparent better performance is somehow related to background noise effects, it is helpful to once again examine a histogram of displacement values. This time, the

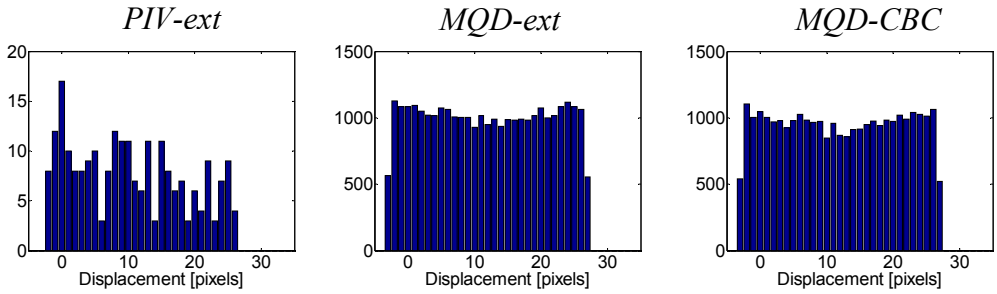

Figure 19: Displacement histogram noise signatures

order of the images in group 01 of data Set A were scrambled in such a fashion that no consecutive images will ever be evaluated at once in the displacement algorithms and a total of 4,000 images were created. There should be, therefore, no correlation between consecutive images in the new scrambled data set and the resulting valid vectors should essentially represent what the algorithm will produce when the input is noisy images with the same characteristics of image group 01 of Set A. All three algorithms were used to analyze this data set.

While MQD-ext and MQD-CBC seem to produce nearly uniform noise across all displacement values, PIV-ext does not (Figure 19). Instead, the valid vectors seem to be slightly more abundant at lower displacement values. Since the mean displacement value is calculated from the sum of all of these valid vectors, the tendency of PIV-ext's vectors to be low will make its mean displacement lower than those calculated by MQD-ext and MQD-CBC (both of which estimated roughly the average of all possible displacement values). With the maximum simulated displacement being 10 pixels, the mean displacement produced by PIV-ext will appear more accurate than the values produced by MQD-ext and MQD-CBC. While it cannot be determined from this simple observation whether the accuracy of PIV-ext at such low SNR levels was due to its dynamic search algorithm or simply due to a

coincidental agreement of the chosen displacement and the inherent noise pattern on the displacement histogram, it certainly highlights an area for further investigation.

3.6 Background Effects

Exploratory tests runs with PIV algorithms analyzing laboratory images indicated that the presence of a strong background gradient in intensity could pose a significant obstacle to successfully obtaining accurate displacement results. Simulated image Set B was created to investigate this effect by adding the same exact background gradient measured on an Omega infrared camera. As stated before, when the thermal surface signature is weak, this background gradient can significantly obscure the visibility. Leaving this background in the images will certainly provide a strong tendency to a zero displacement.

Traditional PIV technicians deal with images in which the particles of interest have been highlighted with external illumination. For this reason, traceable patterns can easily be identified as "hot spots" in the image with intensities *greater* than their surroundings. Cowen and Monismith (1997) deal with this in long data sets by determining the minimum value that is recorded at each pixel over the data set, thus accumulating a comprehensive minimum background image that can be removed. When attempting QI on infrared images, it is understood that parcels of interest are not only discrete hot spots, but also discrete cold spots. Therefore, in order to construct a good estimate of the background image that will be subtracted, each value that is recorded at each pixel in a long data set is held and finally a median value for each pixel is obtained. Due to the size of the images and length of the required data set, this can be an extremely time consuming process.

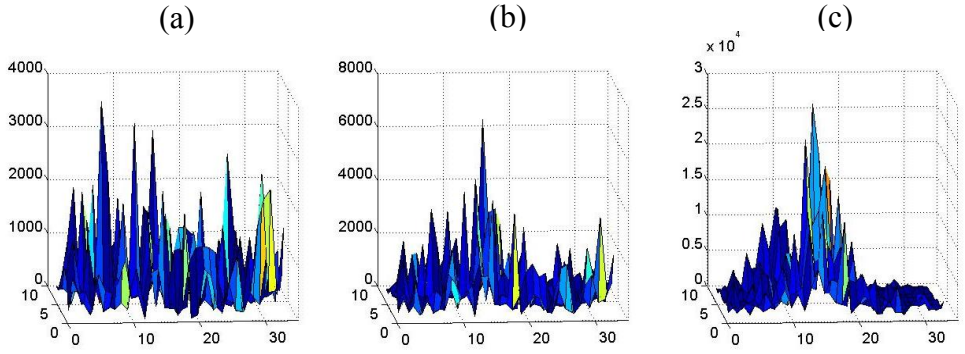

Figure 20: Displacement planes from MQD-CBC on Image Set A (a) Group 2; (b) Group 5; (c) Group 8

This was accomplished on every group of images in Set B. Although the identical background image was added to every image, due to the noise and signal in each image, the resulting median background image may differ slightly. It was hoped that this technique would sufficiently model the noise and random fluctuation of the background image in the laboratory and the field. Unfortunately this did not adequately reproduce the expected adverse affects (the zero-locking phenomenon -- discussed in the next chapter) and the results from the analysis of Set B are nearly identical to those from Set A and will therefore not be presented here.

3.7 Analyzing Low SNR Image Data

Since a primary interest of this thesis is to investigate the effectiveness of these algorithms in low signal strength environments, it is helpful to look further into the results produced for this scenario. Clearly, the accuracy of all three algorithms increases drastically between SNR_{MC} values of 0.1 and 0.4, which corresponds directly to an increased prominence of the peak on each displacement plane (Figure 20). The displacement histograms from all three algorithms taken from the data in this

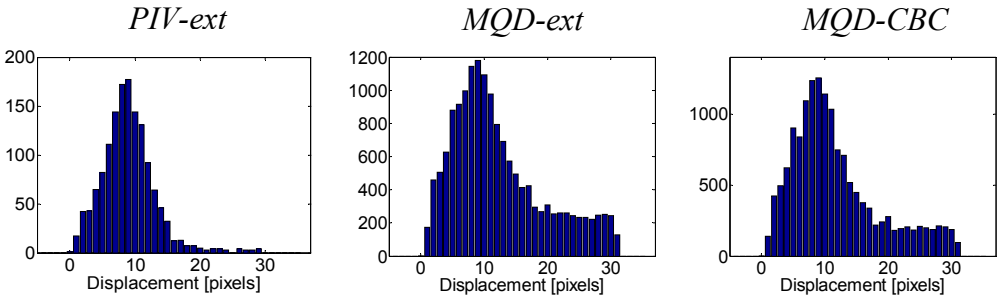

Figure 21: Displacement histograms for Image Set B, Group 5

transitional signal strength range (Figure 21) highlight the effectiveness of the higher-order processing feature (iterative dynamic subwindow searching) available to PIV-ext. The signal is responsible for the peak near the displacement value of 10, while the analysis of noisy image data is responsible for the uniform noise level that appears in the MQD-ext and MQD-CBC histograms. Once again, the non-convergent vector elimination system used in PIV-ext is partially responsible for the shape of that histogram, and it is unclear how much noise was originally present in the histogram. The lack of a uniform noise floor, however, suggests that this dynamic subwindow search algorithm provides superior accuracy for this image group.

3.7 Conclusions

These three displacement algorithms are valuable tools for which to evaluate simulated thermal images of flowing bodies of water. It is clear that they can be used to accurately evaluate images with strong signal. As was expected, PIV-ext was improved upon by the MQD method due to its robustness to noise and pattern intensity variations. The CBC method, while significantly increasing the SNR, made only small improvements to the error and precision of the displacement results. However, the combination of MQD and CBC do, in fact, make for the most accurate

algorithm for analysis of these Monte Carlo Simulation images of sufficiently high SNR_{MC} values.

The other important finding garnered from the comparison of these three algorithms is that although PIV-ext's dynamic subwindow vector elimination method discards nearly 100% of the vectors at extremely low SNR_{MC} (Figure 18), it is not at all clear that the passing vectors are actually valid. Only in the transitional SNR_{MC} range (Figure 21) do we begin to see that this spurious vector elimination system may provide PIV-ext an advantage over the other two MQD based algorithms. Therefore, although we know that, on the whole, the MQD algorithms outperform the PIV algorithm, a reliable method in which to eliminate the noise floor that is currently associated with these displacement histograms must be implemented.

At first glance, it may be obvious to the reader that using an adaptive Gaussian filter would solve this problem easily. While this would be ineffective on the extremely low SNR_{MC} image sets, it *would* be quite effective if used on the results from all three algorithms in the transitional range. Additionally, the implementation of a local median filter (elimination based on the magnitude of a vector's neighbors) is not entirely practical, due to the lack of surrounding vectors. Unfortunately, as will be presented in the next section, the use of the adaptive Gaussian filter becomes ineffective when used in the analysis of real thermal images of a flowing body of water.

CHAPTER 4

EXTRACTING SURFACE VELOCITY PROFILES FROM QUANTITATIVE THERMAL LABORATORY IMAGES

Although the previous chapter depicts that accurate results can be obtained by applying the displacement algorithms to simulated infrared images, proof must also be established that they can adequately extract surface velocity from thermographic laboratory images. The five data sets that were collected in the large flume described in chapter 2 were specifically designed to establish proof that these algorithms can be used to extract surface velocity and ultimately to test the limits of this capability in highly uniform temperature environments. In this chapter the laboratory thermographic images are analyzed with the previously developed displacement algorithms.

4.1 Thermally Disequilibrated Flows

As described in chapter 2, the flow recorded in Data Set 5 was heavily disequilibrated by adding warm water in bulk from the nozzle of a hose. Since the SNR for this image set is sufficiently high, all three of the displacement algorithms perform quite well in extracting the correct surface velocity. For simplicity's sake, only the results from MQD-CBC analysis are presented, as it provided the most precise (i.e. lowest standard deviation) displacement values at high SNR. A detailed quantitative analysis of rms error will not be presented in this thesis. The ADV velocity data was not collected simultaneously with each image set and since the physical act of disrupting the flow with bulk flow from a hose nozzle likely biased the

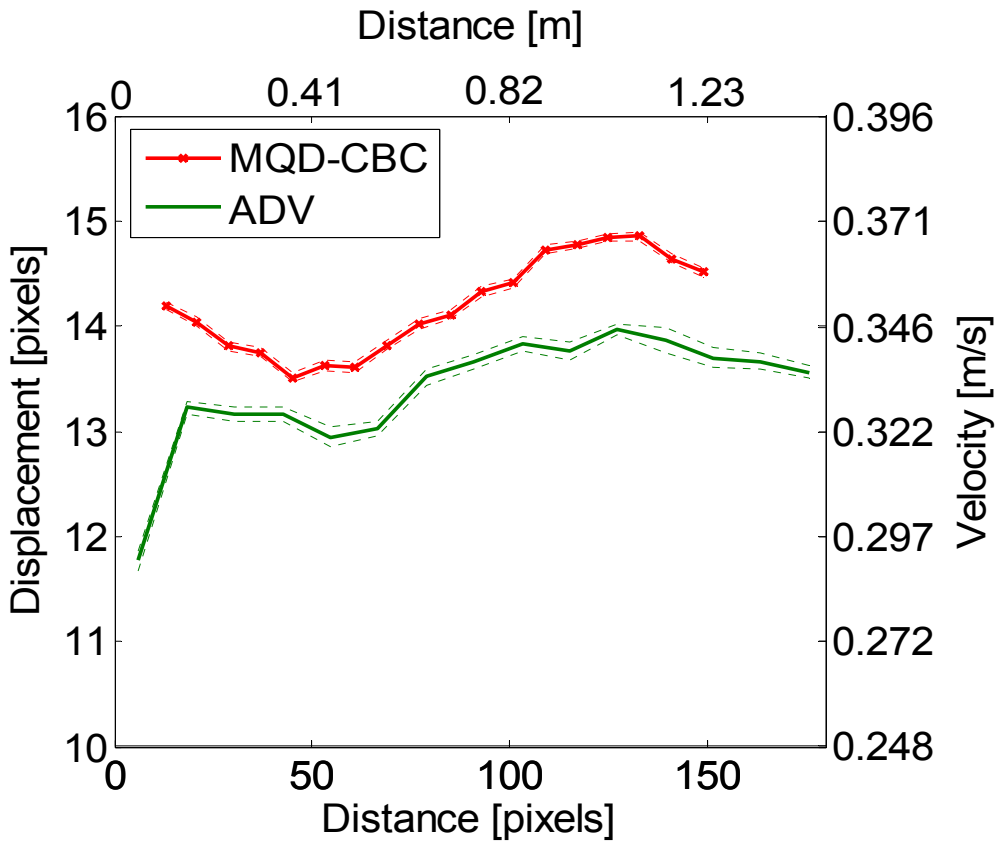

Figure 22: MQD-CBC results for Data Set 5 with 95% confidence intervals shown.

surface velocity, the velocity measurements can only be used as a general estimate of the velocity of the water surface that is seen in the image sets.

Data was collected at a frequency of 30 Hz, and therefore analysis of images taken at lower frequencies can only be accomplished by subsampling the data set. Given the approximate surface velocity recorded by the ADV, subsampling every 10^{th} image of the data set (or a sample rate of 3 Hz) places the expected displacement (roughly 15 pixels) near the center of the displacement plane for MQD-ext and MQD-CBC. The resulting velocity profile (Figure 22) matches the profile recorded with the ADV within nearly 5-10%, and clearly maintains the overall profile shape. Bootstrap

uncertainty intervals of the ADV velocity measurements and MQD-CBC velocity measurements from Data Set 5 are presented in Table 4. Similar results were obtained by varying the subsampling frequency (Figure 23). As is expected, the mean displacement varies linearly with sample frequency and the precision (reciprocally proportional to the variance) and valid vector count both decrease due to STP disintegration as the time between images increases.

Table 4: (a) Uncertainty intervals for ADV velocity measurements; (b) Uncertainty intervals in QI velocity measurements

(a)

Distance from wall [m]	Surface Velocity [m/s]	
0.05	-0.0024	+0.0024
0.15	-0.0016	+0.0015
0.25	-0.0017	+0.0016
0.35	-0.0018	+0.0018
0.45	-0.0022	+0.0025
0.55	-0.0018	+0.0016
0.65	-0.0020	+0.0018
0.75	-0.0018	+0.0017
0.85	-0.0019	+0.0017
0.95	-0.0022	+0.0022
1.05	-0.0014	+0.0015
1.15	-0.0031	+0.0031
1.25	-0.0024	+0.0025
1.35	-0.0017	+0.0018
1.45	-0.0017	+0.0017

(b)

Distance from wall [m]	Surface Velocity [m/s]	
0.11	-0.0030	+0.0030
0.17	-0.0032	+0.0032
0.24	-0.0032	+0.0032
0.31	-0.0035	+0.0032
0.37	-0.0035	+0.0030
0.44	-0.0037	+0.0037
0.50	-0.0040	+0.0037
0.57	-0.0030	+0.0030
0.64	-0.0035	+0.0035
0.70	-0.0035	+0.0032
0.77	-0.0032	+0.0035
0.83	-0.0035	+0.0032
0.90	-0.0037	+0.0030
0.97	-0.0030	+0.0027
1.03	-0.0030	+0.0027
1.10	-0.0032	+0.0032
1.16	-0.0035	+0.0035
1.23	-0.0032	+0.0030

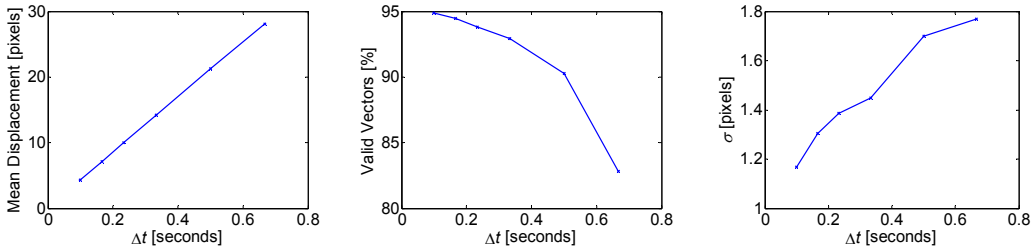

Figure 23: Statistics from MQD-CBC analysis of Data Set 5

The results from Data Set 5 demonstrate the capability of the displacement algorithm to successfully extract a velocity profile from the surface of a flowing body of water, given substantial aid from thermal tagging. Analyses of Data Sets 3 and 4, however, expose the current system's weaknesses, such as the zero-locking phenomenon and sensitivity to noise.

4.2 Zero Locking

Due to the nature of the thermal tagging that took place during Data Sets 3 and 4 (i.e. spray, not bulk flow), the STPs were less distinct, and therefore the SNR was not as high as it was for Data Set 5. Results from these data sets yielded displacement values that were substantially less than the expected values. The reason for this underestimation can be seen in Figure 24, where displacement histograms show that the vast majority of displacement peaks are locking in on a zero-displacement value for both data sets. Note that the significant differences between the two data sets themselves are the distance from the sample area that the flow was tagged. Data Set 3's SNR was much lower due to the extra time that the water had to equilibrate with its surroundings.

The individual displacement planes shed further light on the issue (Figure 25). At low SNR, there exists a sharp one-pixel peak at the zero-displacement location,

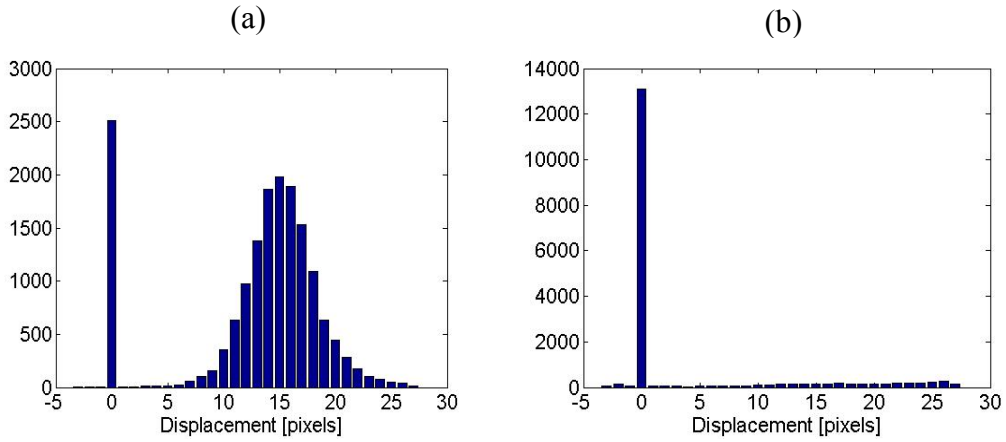

Figure 25: Displacement histograms for Data Sets (a) 3; and (b) 4 both display the "zero lock"

while the rest of the displacement plane is largely shapeless with little evidence of a true displacement peak. As the SNR increases to an intermediate level, it becomes clear that there is a true displacement peak on the displacement plane. However, the zero-displacement peak is still present, and these two peaks often compete closely to set the highest value on the plane. At high SNR, the zero-displacement peak (along with much of the noise) is almost entirely obscured by the signal, resulting in much better algorithm performance

This "zero-locking" phenomenon is a result of the way in which one computes

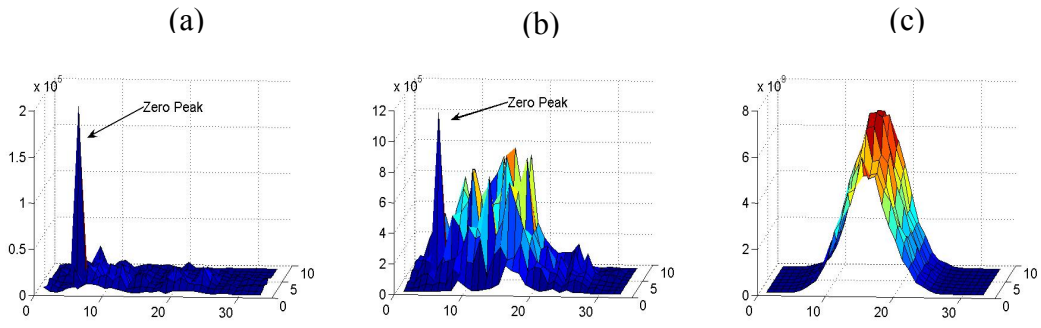

Figure 24: Displacement planes for (a) Low SNR; (b) Medium SNR; and (c) High SNR image sets

and subtracts the background image from a low SNR image set. Unfortunately, there is no perfect method in which to determine exactly what background image a camera and its image environment is imparting on each frame as it is taken. Variables such as background lighting, thermal energy, and temporal variations of pixel response can all make the true background change over time and space during data collection. The experimentalist is forced to estimate this background from the image set itself or by recording a blank image before or after the data collection. In addition to being impractical in the natural environment, using a blank thermal image as the estimated background ignores the potentially significant effects of pixel response variation over time and reflection.

Among other methods, a common way in which to determine the background image while de-weighting outlier pixel intensities is to determine the median temporal value of each pixel over time. While this (and almost any other reasonable method) will work sufficiently in a high SNR environment, it may not perform well in the analysis of low SNR data sets. Since it is extraordinarily unlikely (due to the effects mentioned above) that the background image that is calculated with this method matches exactly the true background image that was recorded by the camera in each frame, there is bound to be a differential image that results from the subtraction of one from the other. Although the differences may be small (+/- 1 integer pixel intensity value), if enough of these small variations exist spatially within the differential image and the SNR is sufficiently low (i.e. ~ 2 – recall that this is the value calculated when analyzing extremely noisy images), this fixed pattern may be prominent enough for the displacement algorithm to mistakenly recognize it as a zero-pixel translation.

Without access to a calibrated blackbody, a thorough study of this camera's background image over time is not possible. Since the spatial and temporal variability of this image is likely the root cause of the zero-locking phenomenon, further research

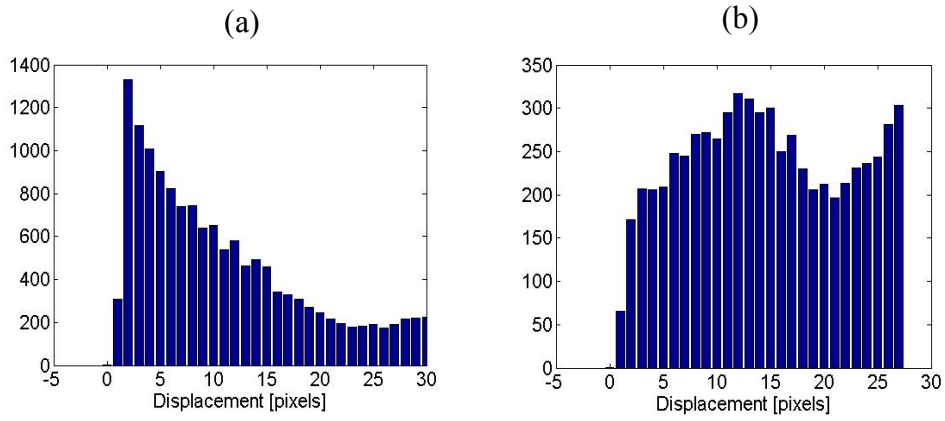

Figure 26: Displacement histograms for Data Set 3 with the (a) median and (b) mean background images subtracted

in this area must be undertaken if one desires the flexibility to extract negative and zero-displacement flows. For the further purposes of this thesis, however, the displacement algorithms have been altered to artificially avoid this issue by only searching for pixel displacements between 1 and 31. Since only positive velocities are expected in these unidirectional flows, this solution is perfectly reasonable, however if, in the future, bidirectional flows are desired, this must be dealt with or higher SNR images must be collected.

The results for Data Set 4 under this new search restriction were comparable to those from Data Set 5, but with slightly less precision (standard deviation of 1.9 pixels per frame). The results from Data Set 3, however, were less clear. Although the displacement histogram (Figure 26 (a)) appears to be trending from high to low displacement, the true displacement signal has been buried by excessive noise in the histogram. This phenomenon is related to the subtraction of the calculated background image and is discussed in the next section when examining the results from Data Sets 1 and 2. Interestingly, when the *mean* background image is removed (as opposed to the median) (Figure 26 (b)), the noise signature changes, and no longer

completely hides the weak displacement signal. Of course, the calculated velocimetry results for Data Set 3 are less than accurate due to the inclusion of the noisy displacement values in the calculation of the mean pixel displacement.

4.3 Equilibrated Flow

To test the limits of this velocimetry method, Data Sets 1 and 2 were evaluated in the same manner as Data Set 3 and 4. These two data sets represent what is expected to be a worst-case scenario as far as temperature distribution and turbulence intensity is concerned. A displacement algorithm that can perform well in this extremely low SNR environment has a much better chance of being successful in all environments that are to be expected in the field. By simply viewing the raw thermographic images (with the median background subtracted – Figure 2), it is obvious that the SNR is on the order of that recorded in the very low SNR_{MC} Monte

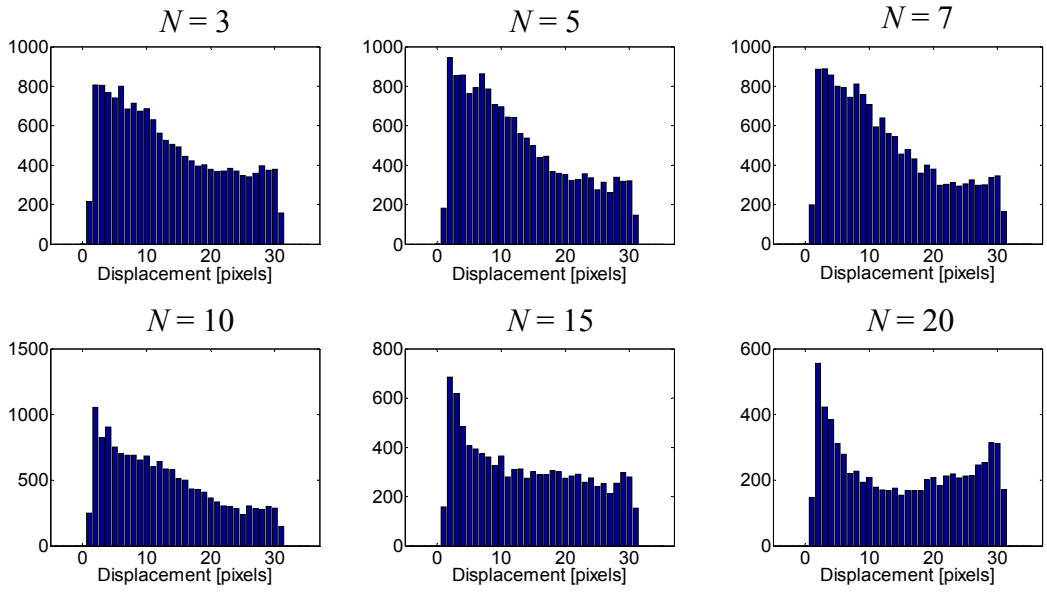

Figure 27: Displacement histograms for Data Set 1 at varying frame rates (where *N* represents analyzing every "*Nth*" image)

Carlo Simulation image sets. It is therefore not surprising that the displacement profile extracted by the displacement algorithm does not match well with the ADV data.

Since the results from Data Sets 1 and 2 are very similar, only Data Set 1 is presented here. The absence of a noise filtering algorithm in MQD-CBC allows a nearly 100% passing rate for the resulting displacement values. Unfortunately, when the SNR is extremely low, this means that the vast majority of these passing values are the result of noise. One may expect that the results from such a noisy data set would produce a uniform field of random displacement values (similar to the way it did in the analysis of Image Set A – Figure 19); however, the displacement histograms from Data Set 1 (Figure 27) suggest otherwise. Although it is clear that a weak signal is hidden behind the noisy results (as is evident from a bulk histogram center of mass shift from left to right as the time between images increases), the overall pattern remains the same.

To further investigate this phenomenon, the images of Data Set 1 were randomly shuffled and duplicated to produce a 10,000 image data set in which no two adjacent images contained shared information. This independent image set was then analyzed by MQD-CBC and the resulting displacement histogram (Figure 28) represents the true "noise signature." This noise signature is not uniform as expected, but instead is biased towards the maximum and minimum possible displacement values, and weighted towards low displacement. This is also evident by examining individual displacement planes (Figure 29), and noting that the general shape matches that of the noise signature. If the edges of the displacement plane are more likely to have peaks than the middle, then the displacement values will be biased towards these areas. Additionally, the signature seems to be directly related to the imaging environment and background images removal method. This process was repeated for

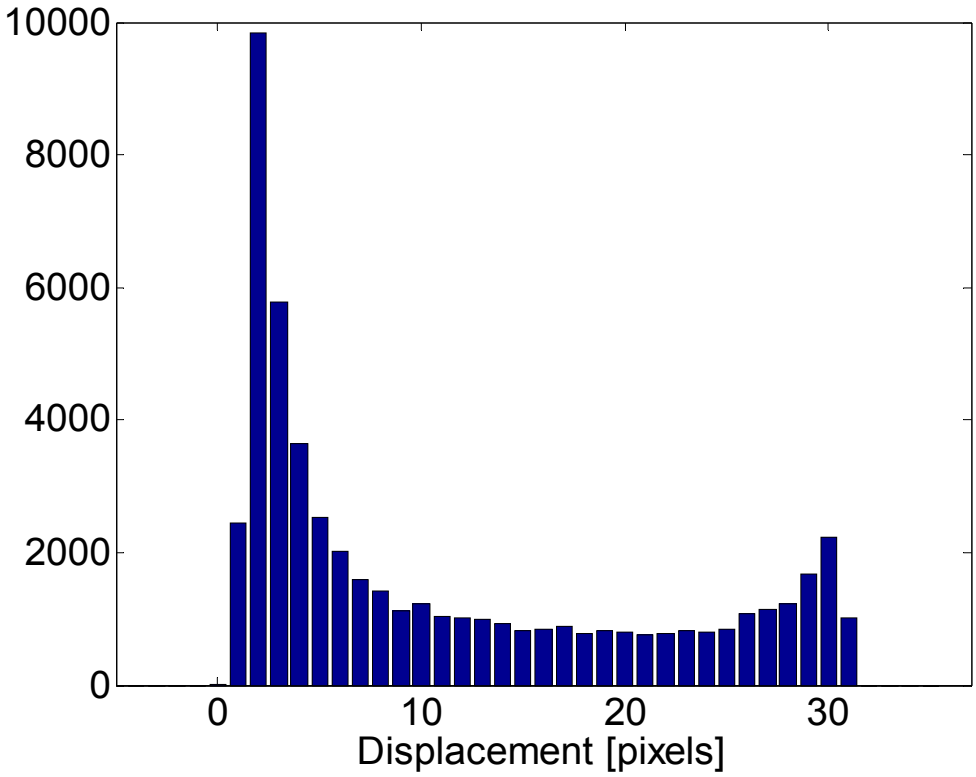

Figure 29: Displacement histogram noise signature from Data Set 1

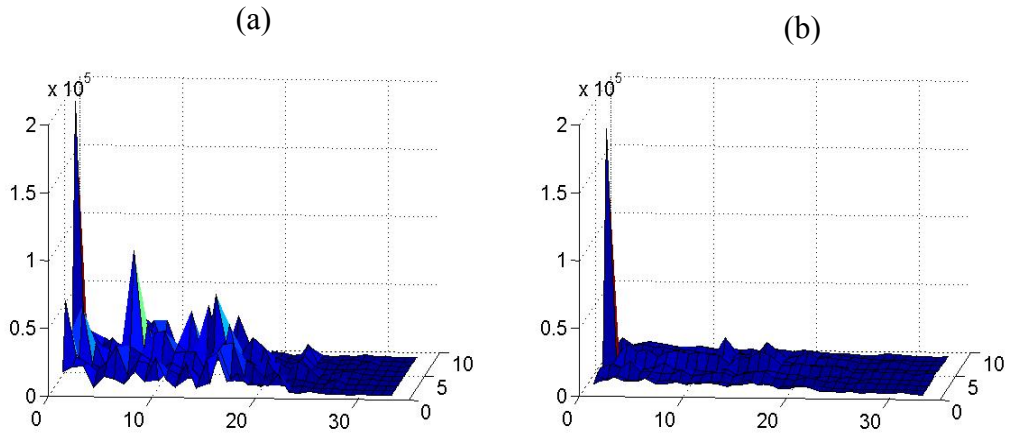

Figure 28: (a) Typical and (b) Mean displacement planes for one image pair from Data Set 1

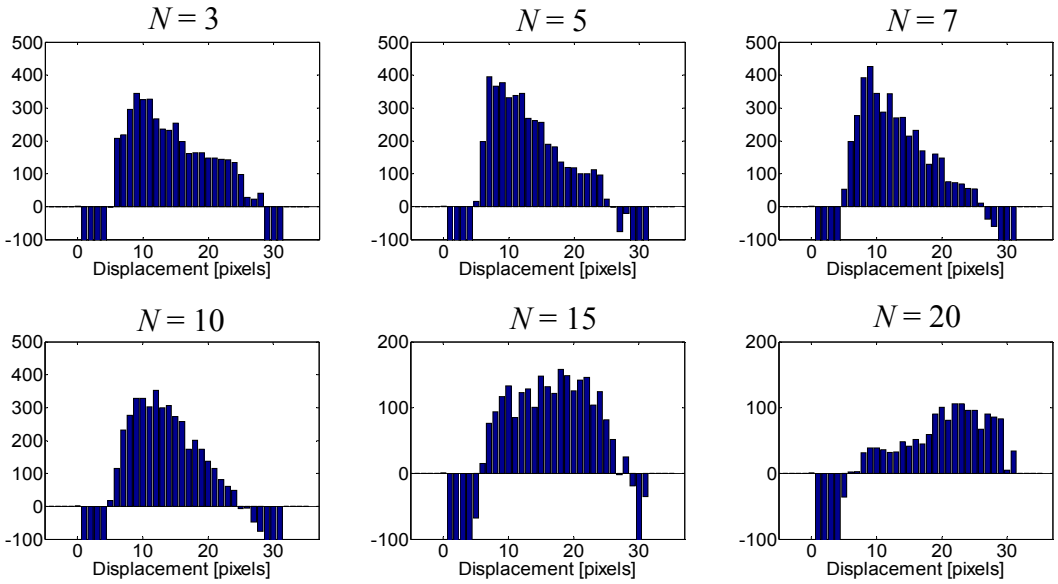

Figure 30: Displacement histograms minus the displacement histogram noise signature for Data Set 1

all of the other data sets and, although the general shape remained the same (i.e. a bias towards the maximum and minimum), the weighting varied. Choosing a different background removal method (i.e. removing the mean, instead of the median image) produced similarly varied results, even from the same data set.

By knowing the true shape of the noise signature unique to an individual data set, one can use it to amplify the existing, but weak signal in each displacement histogram. Borrowing from the very technique used by image acquisitionists to remove the background image effects, we can scale the noise histogram to the size of each individual displacement histogram and then subtract it in the hopes that it will cancel out the noise and leave only the signal. This technique allows us to interpret much more accurate results from Data Set 1 (Figure 30). Although the spread is quite high and the noise subtraction seems to be less effective near the edges, it becomes much more obvious that the peak displacements are near the correct values for their respective time differences (i.e. for $N = 10$ (frequency = 3 Hz), the peak value is near

12-14 pixels, which corresponds to the results from the high SNR Data Set 5). Similar results were reached in the analysis of Data Sets 2 and 3.

4.4 Conclusions

The adapted displacement algorithms developed in Chapter 3 were applied to images of laboratory flows ranging from extremely high to extremely low SNR values. Reliable velocities were extracted from the high SNR image sets and quantitatively verified with non-simultaneous ADV data. The intermediate SNR results revealed the zero-locking phenomenon which was sidestepped by limiting the algorithm search areas to only positive displacement values. With the aid of this limitation, the intermediate SNR image sets also produced reliable and verified velocity results. Analysis of the low SNR image sets helped to establish the non-uniform noise patterns produced by this QI method, and a technique to amplify the weak signal was presented. Although yet to be refined, this technique allowed a favorable qualitative comparison to the ADV data.

CHAPTER 5

CONCLUSION

5.1 Summary and Discussion

Although quantitative imaging techniques have been employed in the recent past (SIV, CIV) to extract fluid velocities from laboratory and field flows, these methods have focused solely on high resolution images taken over a well dispersed scalar with a non-trivial dynamic range. In fact, many of these techniques specifically *rely* on the extremely high integrity of the image data, and even a slightly noisy data set would prohibit reliable results. Since a priority of this project was to keep the cost basis (and hence, the NEdT and resolution) of the thermal imager very low, a system had to be developed that would be robust to a low SNR yet still be able to extract reliable velocities. The first step towards the development of such a system was taken in this thesis and the success of the results from Data Set 5 and the qualified successes of the results from the low SNR data sets prove that the technique satisfies those requirements and is worthy of further research.

The improvements and alterations made to the original PIV algorithm proved to be necessary and valuable. Switching from the correlation based method to the least-squared method clearly improved the accuracy of the results, as did the addition of the CBC method, although to a much lesser degree. Still, further work remains in this area. Developing the ability to identify and discard invalid displacement vectors is of primary importance for further research. Although several different methods have been developed for use in PIV and scalar based quantitative imaging, their effectiveness in such a low SNR environment must be evaluated. Additionally, the

use of techniques such as image convolution, iterative searching algorithms, and other PIV enhancing techniques must be investigated.

In order to properly analyze the aforementioned algorithm improvements, one must also develop an experimental method and/or direct numerical simulations (DNS) that provide a higher degree of control than the ADV verification method and current Monte Carlo Simulations used in this thesis. A data acquisition setup that coupled the experimental techniques developed in this thesis with a surface-seeded CCD camera-based PIV setup would provide the control necessary to verify the accuracy of our method. Alternatively (or in addition), the DNSs that have been developed by gas-transfer researchers would provide the basis to begin testing the algorithm improvements almost immediately.

Further research must also be accomplished in the area of removing the proper image background from the data. Although the current work around of disallowing flow displacements of less than 1 pixel in the positive direction may prove to be the best solution, a more thorough understanding of how the image background changes spatially and temporally will be required in the future in order to maximize the effectiveness of the QI displacement algorithm. Related to this task, the method in which the noise signature is subtracted from the displacement histogram must be refined and tested to verify its accuracy.

This thesis established proof that the proposed technique for extracting a surface velocity profile from thermographic images of a flowing water surface is feasible and promising. However, work remains to be done in order to reliably and accurately extract fluid velocities in the lowest of SNR environments. Several obstacles for future research were identified, and a novel technique in which the noise signature was subtracted from the displacement histogram was introduced. Continued work on this project is clearly justified and could result in the development of a stand-

alone remote sensing system that could change the way in which stream gaging is accomplished in the future.

BIBLIOGRAPHY

B. N. Carpenter and A. J. Pearlstein. Simulation of extraction of velocity from passive scalar data in a two-dimensional diverging channel flow. *Phys. Fluids*, 8(9):2447-2459, 1996.

E. A. Cowen and S. G. Monismith. A hybrid digital particle tracking velocimetry technique. *Experiments in Fluids,* 22:199-211, 1997.

J. D. Creutin, M. Muste and Z. Li. Traceless Quantitative Imaging Alternatives for Free-Surface Measurements in Natural Streams. *Proceedings, ASCE 2002 Hydraulic Measurements and Experimental Methods Conference*, Estes Park, CO July 28 – August 01, 2002.

W. J. A. Dahm, L. K. Su and K. B. Southerland. A scalar imaging velocimetry technique for fully resolved four-dimensional vector velocity field measurements in turbulent flows. *Phys. Fluids*, 4(10):2191-2208, 1992.

I. Fujita and R. Tsubaki. A Novel Free-Surface Velocity Measurement Method Using Spatio-Temporal Images. *Proceedings, ASCE 2002 Hydraulic Measurements and Experimental Methods Conference*, Estes Park, CO July 28 – August 01, 2002.

C. S. Garbe, H. Spies and B. Jähne. Estimation of Surface Flow and Net Heat Flux from Infrared Image Sequences. *Journal of Mathematical Imaging and Vision, 19:159-174, 2003.*

L. Gui and W. Merzkirch. A comparative study of the MQD method and several correlation-based PIV evaluation algorithms. *Experiments in Fluids,* 28:36-44, 2000.

R. A. Handler, G. B. Smith and R. I. Leighton. The thermal structure of an air-water interface at low wind speeds. *Tellus Series A-Dynamic Meteorology and Oceanography*, 53 (2):233-244, 2001.

D. P. Hart. PIV error correction. *Experiments in Fluids,* 29:13-22, 2000.

H. Haussecker, U. Schimpf, C. S. Garbe and B. Jähne. Physics from IR Image Sequences: Quantitative Analysis of Transport Models and Parameters of Air-Sea Gas Transfer. *Gas Transfer at Water Surfaces*, pages 103-108, 2002.

G. Hetsroni, T. A. Kowelewski, B. Hu, and A. Mosyak. Tracking of coherent thermal structures on a heated wall by means of infrared thermography. *Experiments in Fluids,* 30:286-294, 2001.

M. C. Lee, C. J. Lai, J. M. Leu, W. J. Plant, W. C. Keller and K. Hayes. Non-contact flood dischare measurements using an X-band pulse radar (I) theory. *Flow Measurement and Instrumentation*, 13:265-270, 2002.

M. C. Lee, J. M. Leu, C. J. Lai, W. J. Plant, W. C. Keller and K. Hayes. Non-contact flood dischare measurements using an X-band pulse radar (II) Improvements and applications. *Flow Measurement and Instrumentation*, 13:271-276, 2002.

Q. Liao. *An Experimental Investigation of Plume Dispersion in a Turbulent Boundary Layer and Implications for Plume Tracing*, Cornell University, 2004.

R. R. Mason, J. E. Costa and R. T. Cheng. A Proposed Radar-Based Streamflow Measurement System for the San Joaquin River at Vernalis, California. *Proceedings, ASCE 2002 Hydraulic Measurements and Experimental Methods Conference*, Estes Park, CO July 28 – August 01, 2002.

A. Mosyak and G. Hetsroni. Visual study of bursting using infrared technique. *Experiments in Fluids, 37*:40-46, 2004.

K. R. Nicolas, W. T. Lindenmuth, C. S. Weller, D. G. Anthony. Radar imaging of water surface flow fields. *Experiments in Fluids,* 23:14-19, 1997.

A. J. Pearlstein and Bonnie N. Carpenter. On the determination of solenoidal or compressible velocity fields from measurements of passive or reactive scalars. *Phys. Fluids*, 7(4):754-763, 1995.

G. Quenot. The “Orthogonal Algorithm" for Optical Flow Detection using Dynamic Programming. *IEEE International Conference on Accoustics, Speech and Signal Processing*, San Francisco, CA, USA, March 1992.

L. K. Su and W. J. A. Dahm. Scalar imaging velocimetry measurements of the velocity gradient tensor field in turbulent flows. I. Assessment of errors. *Phys. Fluids*, 8(7):1869-1882, 1996.

L. K. Su and W. J. A. Dahm. Scalar imaging velocimetry measurements of the velocity gradient tensor field in turbulent flows. II. Experimental results. *Phys. Fluids*, 8(7):1883-1906, 1996.

P. T. Tokumaru, P. E. Dimotakis. Image correlation velocimetry. *Experiments in Fluids,* 19:1-15, 1995.

V. Weitbrecht, G. Kühn and G. H. Jirka. Large scale PIV-measurements at the surface of shallow water flows. *Flow Measurement and Instrumentation*, 13:237-245, 2002.